universität wien

MASTERARBEIT | MASTER'S THESIS

Titel | Title

Global Emission Estimates of Tetrafluoromethane (CF_4) determined by Inverse Modelling

verfasst von | submitted by

Luise Elisabeth Kandler B.Sc.

angestrebter akademischer Grad | in partial fulfilment of the requirements for the degree of

Master of Science (MSc)

Wien | Vienna, 2025

Studienkennzahl lt. Studienblatt | Degree programme code as it appears on the student record sheet:	UA 066 299
Studienrichtung lt. Studienblatt | Degree programme as it appears on the student record sheet:	Masterstudium Environmental Systems: Processes - Pollution - Solutions
Betreut von | Supervisor:	Univ.-Prof. Mag. Dr. Andreas Stohl

Abstract

Tetrafluoromethane (CF_4) is a potent greenhouse gas with an atmospheric lifetime of approximately 50,000 years and an extremely high global warming potential (Burkholder et al., 2019). Although CF_4 is known to be primarily emitted by the aluminum and semiconductor industries (Kim et al., 2014), bottom-up inventories based on industry-reported data were found to be highly uncertain, with both global and regional top-down studies consistently indicating substantially higher emissions (Kim et al., 2021). As a result, reported emission values are likely underestimated, which may contribute to CF_4's insufficient regulation in national and international climate frameworks. To date, top-down studies have offered only limited spatial coverage and resolution, even in high-emission regions such as South and East Asia, Europe, and North America. To address these limitations, we applied the FLEXINVERT+ Bayesian inversion framework (Thompson & Stohl, 2014) on a global domain using all available atmospheric flask and in situ measurements from 2006 to 2023 to obtain regionally resolved CF_4 emission estimates for the whole globe.

Despite regional variability in uncertainty, our approach provides the first top-down estimates for major emitters such as Russia, India, South and East Asia, and the entire European continent, while also refining estimates over known hotspots including China, North America, and Northwest Europe through the integration of recently published observation data. Given that the inversion's reliability is strongly dependent on the spatial and temporal density of atmospheric observations, the model performs particularly well in well-observed areas between 2007 and 2021 with global uncertainty reductions reaching up to 40%. Our results support previous findings, showing that total posterior emissions exceed prior estimates in 65–85% of country-level contributions. China exhibits the largest discrepancies, accounting for up to 60% of the global bottom-up to top-down difference, while regions with more established regulatory frameworks, such as the United States (U.S.) and the European Union (EU), display closer agreement between top-down and bottom-up estimates. Our global emission trend indicates an approximate 32% increase from 2007 to 2021, with temporal variability reflecting global and regional political-economic developments and technological transitions. Country-specific trends identify China as the dominant emitter with a consistent upward trend, contributing over 50% of global emissions throughout most of the study period. In contrast, established emission hotspots such as Europe, North America, Russia, and Tajikistan exhibit stable or declining emission trends. On the other hand, despite inherent uncertainties, our results suggest the emergence of new emission contributors in recent years, notably India, Malaysia, and Vietnam. These findings all together expose significant structural deficiencies in existing inventories and underscore the necessity of integrating top-down approaches for accurate emission quantification and trend detection. Given the extreme persistence and high global warming potential of CF_4 (Burkholder et al., 2019), enhanced measurement networks and improved reporting are crucial to inform and support effective climate mitigation policies.

Zusammenfassung

Tetrafluormethan (CF_4), das hauptsächlich als Nebenprodukt der Aluminium- und Halbleiterindustrie emittiert wird, ist ein äußerst potentes Treibhausgas mit einer atmosphärischen Verweildauer von etwa 50.000 Jahren und einem extrem hohen Treibhauspotenzial (Burkholder et al., 2019; Kim et al., 2014). Bottom-up-Emissionsinventare auf Basis industrieberichteter Daten sind meist mit erheblichen Unsicherheiten behaftet. Sowohl globale als auch regionale Top-Down-Studien deuten auf deutlich höhere Emissionen hin (Kim et al., 2021). Folglich sind national und international veröffentlichte Bottom-Up Emissionswerte vermutlich signifikant unterschätzt, was die aktuell unzureichenden Regulierung von CF_4 sowohl auf nationaler als auch internationaler Ebene begünstigt.

Da bisherige Top-Down-Studien keine flächendeckende globale Auflösung aufweisen und selbst in emissionsstarken Regionen wie Ostasien, Europa und Nordamerika lückenhaft sind, nutzen wir in unserer Studie das Bayes'sche Inversionsmodell FLEXINVERT+ (Thompson & Stohl, 2014) mit sämtlichen verfügbaren atmosphärischen Messdaten im Zeitraum von 2006–2023, um erstmals räumlich aufgelöste globale Top-Down-Emissionsschätzungen von CF_4 zu erhalten. Trotz regional variierender Unsicherheiten im Modell, liefert unser Ansatz erstmals Top-Down-basierte Emissionsschätzungen für Emissions-Hotspots wie Russland, Indien, Süd- und Ostasien sowie den gesamten europäischen Kontinent. Gleichzeitig ermöglichen neu integrierte Messdaten aktualisierte Schätzungen in bekannten Emissions-Gebieten wie China, Nordamerika und Nordwesteuropa. Die Performance der Inversion hängt stark von der räumlich-zeitlichen Dichte der verfügbaren Beobachtungsdaten ab und ist besonders im Zeitraum von 2007–2021 hoch, was globale Unsicherheiten in Bottom-Up Schätzungen bis zu 40% reduziert hat. Wie schon in früheren Studien hervorgehoben, weisen auch unsere Ergebnisse modellierte Emissionen auf, die zu 65–85 % über den jeweiligen Bottom-Up Schätzungen liegen. China weist dabei die größten Abweichungen auf und trägt bis zu 60 % zur globalen Differenz zwischen Bottom-Up- und Top-Down-Schätzungen bei. Regionen mit mehr etablierten Mess- und Reporting-Netzwerken, wie etwa die USA und die EU zeigen hingegen eine deutlich bessere Übereinstimmung zwischen Top-Down- und Bottom-Up-Ergebnissen. Unser globaler Emissionstrend zeigt einen Anstieg von etwa 32 % im Zeitraum von 2007 bis 2021, wobei zwischenzeitliche Schwankungen politische, wirtschaftliche und technologische Entwicklungen auf globaler und regionaler Ebene widerspiegeln. Länderspezifische Analysen identifizieren China als Hauptemittenten mit einem konsistenten Anstieg der Emissionen und globalen Beiträgen von meist über 50 %. Im Gegensatz dazu zeigen etablierte Emissionsregionen wie Europa, Nordamerika, Russland und Tadschikistan stabile bis rückläufige Trends. Auf der anderen Seite, deuten Ergebnisse der letzten Studienjahren, zwar mit höheren Unsicherheiten, auf neue Emissionsgebiete wie Indien, Malaysia und Vietnam hin. Insgesamt offenbaren unsere Ergebnisse erhebliche strukturelle Defizite in Bottom-Up-Inventaren und unterstreichen die Notwendigkeit, Top-Down-Studien zur präzisen Quantifizierung und Verfolgung von Emissionstrends stärker in nationale und internationale

Berichte zu integrieren. Angesichts der extremen Langlebigkeit und des hohen Treibhauspotenzials von CF_4 (Burkholder et al., 2019) sind der Ausbau atmosphärischer Messnetze sowie eine verbesserte Emissionsberichterstattung essenziell, um effektive klimapolitische Maßnahmen zu unterstützen.

Table of Contents

1. State of Research and Political Context

1.1. Greenhouse Gas Emissions and Climate Change

The atmosphere, with all its components and physio-chemical influences, serves as a powerful global transport system and a major sink for pollutants, making it a crucial driver of climate change. Limiting anthropogenic contributions to climate change has become an urgent global priority, with a strong focus on greenhouse gases (GHGs). In contrast to well-studied greenhouse gases such as carbon dioxide (CO_2) and methane (CH_4), emissions of fluorinated gases like tetrafluoromethane (CF_4) have received less attention, despite being crucial to detect, regulate, and reduce in order to curb high-emission processes and mitigate global warming.

1.2. The Importance of Accurate CF_4 Emission Estimates

Tetrafluoromethane, also known as PFC-14, R-14, or CF_4 is the smallest, simplest, and most abundant Perfluorocarbon (PFC) (Arnold et al., 2018). It is structurally similar to methane but with all hydrogen atoms replaced by fluorine atoms. The fluorine-carbon covalent bond is one of the strongest covalent bonds in chemistry making CF_4 extremely stable and inert resulting in an atmospheric lifetime of approximately 50,000 years (Burkholder et al., 2019). With its extremely long persistence, CF_4 is the longest-lived greenhouse gas (GHG) and has a global warming potential over 500 years (GWP_{500}) 10,000 times higher than that of CO_2 (Intergovernmental Panel on Climate Change (IPCC), 1995, p. 19). It is important to note, however, that even GWP_{500} does not fully capture the long-term impact of CF_4, as the gas remains in the atmosphere for well beyond 500 years, with much of its warming effect occurring after this relatively short time window given the timescale.

Although fluorinated gases only accounted for about 2% of total greenhouse gas emissions (GtCO2 eq/yr) in 2019, their exceptionally high GWP makes them significant contributors to global warming (Intergovernmental Panel on Climate Change, 2022). CF_4 is unique among PFCs as it is naturally released from calcium fluorite (CaF_2) of the continental crust leading to a stable pre-industrial background concentration of 34.1 ± 0.3 ppt (Trudinger et al., 2016). However, since the beginning of the Anthropocene, CF_4 emissions have increased sharply due to industrial activities. The aluminum smelting industry has been identified as the dominant anthropogenic source, responsible for approximately 68% of global emissions in 2010 (Kim et al., 2014). Anode effects in aluminum smelting lead to unintended carbon-fluorine bond formation, whereby high anode effect frequency and prolonged duration significantly increases CF_4 emissions (Leber et al., 2016). Modern smelters with improved process control have already significantly reduced CF_4 emissions (Wong et al., 2015). Additional sources include chemical cleaning agents, flat panel display production, plasma etching processes of

semiconductor production, and electrolysis processes in the rare-earth metal industry, which has been associated with recent increases in emissions (Cai et al., 2018; Harnisch, 2000; Kim et al., 2021; Say et al., 2021). Recent research has additionally identified a previously unrecognized atmospheric photochemical source of CF_4. A study by *Jubb et al. (2015)* found that atmospheric decomposition of certain Hydrofluorocarbons (HFCs) through photolysis produces small but measurable amounts of CF_4 (Jubb et al., 2015). While CFC-114a shows the greatest per molecule CF_4 production among the studied halocarbons, HFC-134a is yet the greatest source of CF_4 due to its high atmospheric abundance. However, total photochemical contribution is minor compared to industrial sources (Jubb et al., 2015).

CF_4 removal from the atmosphere is generally highly inefficient and negligible over time scales of hundreds to a few thousand years. Atmospheric degradation processes in the troposphere and stratosphere through reactions with other atmospheric gases are mostly non-exothermic and thus impossible under atmospheric conditions or nearly impossible due to insufficient solar activating energy, such as photolysis or oxidative reactions with OH or ozone (Cicerone, 1979). Its low solubility in water also makes the ocean an insufficient sink. Even if fully saturated, it would hold less than 0.2% of atmospheric CF_4 (Cicerone, 1979). These findings are supported by a recent study of *Li and Tanhua (2021)* using new aquatic measurement techniques that found aquatic CF_4 concentrations to be below detection limit (P. Li & Tanhua, 2021). Accordingly, the same applies to precipitation. If fully saturated with CF_4, at a rate of 1 m/y, precipitation would only remove around 0.00002% of atmospheric CF_4 annually (Cicerone, 1979). High-temperature combustion is as well ineffectively slow and biological degradation processes are not known at all. The only known atmospheric sink is vacuum ultraviolet (VUV) radiation in the high mesosphere and ionosphere, with possible minor contributions from cosmic rays (Cicerone, 1979).

Compared to other GHGs, CF_4 has received relatively little attention in policy and climate research. Its long lifetime however means that even small emissions lead to atmospheric accumulation, with observed concentration increases reaching 0.9 ppt per year as of 2019 (Arnold et al., 2018). Given its persistence and potency, precise emission estimations are essential for highlighting the role of CF_4 as a contributor to global warming and support effective climate agreements.

1.3. Political Frameworks on Emission Monitoring, Reporting and Reduction

Inspired by the success of the *Montreal Protocol (1987)* which successfully banned ozone-depleting substances (ODS), like chlorofluorocarbons (CFCs) or hydrochlorofluorocarbons (HFCs) (United Nations Environment Programme (UNEP), 1987), the *United Nations Framework Convention on Climate*

Change (UNFCCC, 1992) forms the global frame for international agreements on the emission of greenhouse gases and climate change (United Nations Framework Convention on Climate Change, n.d.). It is supported by the *Intergovernmental Panel on Climate Change (IPCC, 1988)* providing scientific assessment reports (e.g. AR5, 2014 or AR6, 2021) (Intergovernmental Panel on Climate, 2024). 198 countries, including the U.S., China, and the EU, are parties of the UNFCCC. Depending on their state of industrialization, countries are subjected to stricter (Annex-I) or less strict (Non-Annex-I) reporting obligations (United Nations Framework Convention on Climate Change (UNFCCC), 2025). Annex-I countries have to report direct GHG emissions and removals including PFCs like CF_4 in a yearly report.

The first legally binding agreement under the UNFCCC was the *Kyoto Protocol (1997)* setting general emission reduction targets for greenhouse gases (United Nations Framework Convention on Climate Change, 1997). Within the first commitment period from 2008–2012 the average individual reduction target of Annex-I countries was at least 5% below 1990 levels which was followed by a second phase from 2013–2020 (Doha Amendment) with more flexible targets aiming a reduction of 18% below 1990 levels by Annex-I countries (United Nations Framework Convention on Climate Change (UNFCCC), 2012).

The Montreal and the Kyoto protocol as first international frames led to several national efforts. As a mitigation strategy the EU introduced the *Emission Trading Scheme (EU ETS)* in 2005 (European Union, 2003) and the first *F-Gas Regulation* in 2006 updated in 2014 and 2024 with more ambitious reduction targets mandating a complete phase out of HFC consumption by 2050 and a reduction in production to 15% of baseline levels by 2036 (European Parliament Council, 2024; European Union, 2014, p. 51). In the U.S. the *United States Environmental Protection Agency (EPA)* has launched the *Clean Air Act (CAA) Amendments* (United States Congress, 1990) followed by the *Significant New Alternatives Policy (SNAP) program* (U.S. Environmental Protection Agency, 1994) regulating ODS alternatives like certain HFCs and PFCs. However, since CF_4 was not a primary substitute of these substances, it is only being monitored and reported under the EPA's *Greenhouse Gas Reporting Program (GHGRP)* (U. S. Environmental Protection Agency (EPA), 2009) since 2010. Nevertheless, the *Voluntary Aluminum Industrial Partnership (VAIP) Program (1995-2015)* achieved a 30%-60% PFC-reduction by EPA partner companies in 2000 compared to the 1990 baseline (U. S. Environmental Protection Agency (EPA), 1995). Developing nations like China, India, and Malaysia had less obligations despite their high emissions. China's monitoring programs including CF_4 were first addressed in its *12th Five-Year Plan* in 2011 (China's National People's Congress, 2011).

Since the withdrawal of several high emitting countries like the U.S., Canada and Japan from the *Kyoto Protocol* after the first commitment period, new efforts have been made with the introduction of the *Paris Agreement* in 2015 (United Nations Framework Convention on Climate, 2015; United Nations Framework Convention on Climate Change (UNFCCC), 2012). The *Paris Agreement (2015)* entered

into force in 2016 replacing the legally binding targets of the *Kyoto Protocol* with voluntary *Nationally Determined Contributions (NDCs)* updated every five years by all 194 countries, allowing countries to set their own climate and emission targets (United Nations Framework Convention on Climate, 2015). It generally encourages fluorinated gas mitigation strategies, while the additional *Kigali Amendment (2016) to the Montreal Protocol*, which entered into force in 2019, specifies at least a HFC phase-out (United Nations Environment Programme (UNEP), 2016).

After signing and ratifying the *Paris Agreement* as well as the *Kigali Amendment* in 2016 China has submitted *China's 13th Five-Year Plan on Ecological and Environmental Protection (2016)*, which states to introduce a more unified monitoring system of multiple pollutants and an emission permit system (Government of the People's Republic of China, 2016) later realized as *China's emissions trading system (2021)* (International Carbon Action Partnership (ICAP), 2024). The EU further launched the *European Green Deal* in 2019 addressing general F-Gas reduction targets and agreed on European climate law in 2021 (European Commission, 2019b; European Parliament and Council, 2021). Despite its existing structures, recent commitment to international frames by the U.S. has been politically controversial with a temporal withdrawal from the *Paris Agreement* under president Trump (2017–2021) and the latest withdrawal in 2025.

In general, international as well as national emission agreements of high emitting countries reveal a lack of concrete restrictions on PFCs and CF_4 in particular. While CF_4 monitoring has improved over the last decade, it still lacks global coverage including some major emitting countries. The *IPCC Assessment Reports* additionally emphasize discrepancies between reported and actual emissions underlining the need for more accurate CF_4 emission estimations (IPCC, 2014).

1.4. Bottom-Up vs. Top-Down Approaches of Emission Estimates

Accurate CF_4 emission estimates are hindered by the lack or difficulties in measuring emissions directly with high spatial and temporal resolution and full global coverage. Hence, bottom-up methods are widely used, which estimate emissions based on reported national or sectoral activity data (e.g. production, consumption) and corresponding emission factors (including e.g. the mix of technologies and abatement measures). Since these factors, coming with their own uncertainties, scale emissions only to broad regions or sectors and generally only account for known emission sources, bottom-up inventories are vulnerable to underreporting of emission magnitude and unaccounted sources. This can result in discrepancies to actual emissions by factors of two or more in the case of industrial greenhouse gases as well as limited spatial resolution (Nisbet & Weiss, 2010; Weiss & Prinn, 2011).

While, bottom-up estimates serve as a prior guess, top-down approaches additionally use atmospheric measurements combined with atmospheric transport models and inversion frameworks to refine bottom-

up emission estimates. In contrast to bottom-up estimates, the addition of frequent observations and the application of inverse modeling tools allows for independent verification of emission magnitudes and distribution, and potentially even for identification of unknown sources. However, top-down approaches come with their own uncertainties, particularly those driven by errors in transport modeling and inversion (see section 2.6.), as well as by sparse observation networks. Additionally, top-down approaches face challenges in attributing emissions to specific sectors or activities. Nevertheless, top-down techniques have repeatedly shown that atmospheric concentrations of some greenhouse gases exceed those reported by bottom-up inventories (Nisbet & Weiss, 2010; Weiss & Prinn, 2011).

Combining bottom-up and top-down approaches is essential for improving the accuracy of emission inventories. Frameworks that refine primary bottom-up emission estimates by using measurement data of observation networks, transport models such as the *FLEXible PARTicle dispersion model* (*FLEXPART)*, and its inversion tool FLEXINVERT+ help reconcile discrepancies and identify unreported or underestimated sources. As shown by Weiss & Prinn (Weiss & Prinn, 2011), top-down approaches can serve as a crucial verification tool for bottom-up inventories in well-observed areas, while bottom-up estimates remain crucial as a primary constraint especially in less observed areas.

Since international and national climate agreements currently lack specific restrictions or monitoring obligations for CF_4, improving the measurement and modeling infrastructure is important to enhance verification systems, help identify overlooked or misreported emissions, and support more effective regulatory frameworks (Mühle et al., 2010).

1.5. Current State of Research on CF_4 Emissions

1.5.1. Early Measurements and Emission Estimates

Early studies on CF_4 emissions started with bottom-up approaches to estimate CF_4 levels and sources. The EPA with its *VAIP Program* (U. S. Environmental Protection Agency (EPA), 1995) sponsored one of the first studies by *Leber et.al. (1998)* who investigated if aluminum smelter characteristics and operating parameters could be used for bottom-up PFC emission predictions and mentioned anode effect frequency and duration to play a crucial role (Leber et al., 2016). Two years later *Harnisch (2000)* used early bottom-up estimates from industrial production reports and early atmospheric measurements highlighting the long atmospheric lifetime of CF_4 and its persistence in the environment (Harnisch, 2000). In the same year *Prinn et al. (2000)* published one of the first long-term datasets of multiple GHGs derived from a global network of air sampling stations of the *Advanced Global Atmospheric Gases Experiment (AGAGE)* providing in-situ atmospheric measurements (Prinn et al., 2000). The introduction of a new measurement technique with improved accuracy in 2004 enabled PFC in-situ measurements with CF_4 measurements starting in 2006. Initially tested at Mace Head (MHD) and Cape

Grim (CGO) observation sites, the introduction of PFC measurement techniques expanded to a continuously growing observation network (see section 3.2.) (Mühle et al., 2010; Prinn et al., 2022).

1.5.2. Development of Top-Down Approaches and Improvement of Bottom-Up Estimates

The availability of continuous in-situ measurement data by AGAGE lead to first top-down approaches using observational data to model global, regional or sector specific emissions and reveal gaps in bottom-up approaches.

In 2010 *Mühle et. al (2010)* used ice cores and firn air measurements to determine CF_4 background and baseline growth rates from the 1970s until 2010 as well as recent AGAGE in-situ observations (of THD, CGO, MHD, RPB, SMO) for global top-down estimates with the *AGAGE 2-D 12-box model* estimating the global source strength of CF_4. Their study revealed interhemispheric gradients as well as discrepancies between observed concentrations and probably underestimated reported emissions emphasizing the need for top-down verification (Mühle et al., 2010). A similar approach was later used by *Trudinger et. al. (2016)* who used historical ice core and firn air samples and the *2-D 12-box AGAGE atmospheric transport model* to apply two different inversion models. Global emission peaks and drops in the resulting atmospheric CF_4 abundance between 1800 and 2014 were linked to possible major events in policy, economy and industry (Trudinger et al., 2016). An analysis of the first in situ continuous observation site in China (SDZ) was performed by *Yao at al. (2012)* in 2012 who used FLEXPART for backward trajectory calculations highlighting the need for additional observation sites in South China (Yao et al., 2012). First continuous atmospheric air samples from 2004 to 2010 measured at AGAGE stations near industrial sites in Australia (CGO) and South Korea (GSN) were used by *Kim et al. (2014)* for an air mass back trajectory analysis of sector specific emissions revealing higher measured emissions than reported by aluminum and semiconductor industries and calling for improvement of site-specific emission factors (Kim et al., 2014). A subsequent study one year later by *Wong et.al. (2015)* reveals previously unrecognized PFC emission processes in the aluminum industry which may have caused significant under-accounting of PFC emission factors by the aluminum industry from 2006–2010 and could explain the previously noticed discrepancies between bottom-up reports and AGAGE observations (Wong et al., 2015). In 2018 *Cai et.al. (2018)* complemented bottom-up inventories with previously unaccounted CF_4 emissions from rare earth metal processing using direct air samples of exhaust gases from China's rare earth metal industry and thereby further improved bottom-up emission factors (Cai et al., 2018).

1.5.3. Recent Inversion Approaches reveal Global and Regional Trends

With continuously improving bottom-up estimations and a growing number of measurements, inversion approaches are constantly refined and reveal trends and gaps. A regional study of *Arnold et. al. (2018)* on East Asian CF_4 emissions used atmospheric measurements from the South Korean Gosan (GSN) station (2008–2015) and the *Numerical Atmospheric dispersion Modelling Environment (NAME) model* in combination with a Bayesian inversion framework. Due to limited prior emission estimations and a significant influence of atmospheric measurements the study mainly identified emission hotspots near the measurement site in South Korea (Arnold et al., 2018). A similar study of *Kim et. al. (2021)* further refined East Asian CF_4 emissions using more recent data from Gosan station (2009-2019) as well as more detailed prior information of national and sector-specific bottom-up reports combined with scaling efforts by population and industry distribution. Using the Bayesian inversion framework FLEXINVERT+ they found that Chinese emissions occur predominantly from the aluminum industry with significant contributions from Japan's and Korea's semiconductor industry, which seem to underestimate their bottom-up emissions (Kim et al., 2021). With a continuous historical analysis of China's F-Gas emissions from 1990 – 2019 combining a broad range of bottom-up and top-down results of previous studies and reports *Guo et.al. (2023)* provided refined bottom-up emission estimates and future predictions of China's F-Gas emissions until 2060. Their results emphasize the potential of Chinese F-Gas emissions to equal or even exceed 2060 CO_2 emissions in China calling for urgent restrictions (Guo et al., 2023). The most recent study on CF_4 emissions of the East Asia region by *An et. al. (2024)* significantly refined top-down emission estimations by providing new long term observations from 2011 – 2021 from nine sites within the Chinese mainland filling measurement gaps of global relevance in this high emitting region. Their new data analysis with the *NAME dispersion model* and a Bayesian - Monte Carlo (HBMCMC) based inversion reveals the spatial distributions of emissions in China and proposes Chinese CF_4 emissions to account for ~ 42 - 66% of global total emissions in the studied years (An et al., 2024).

Despite the great focus of recent research on East Asian or Chinese emissions respectively, recent studies also include latest emission estimations for Australia and Europe as well as global trends. The observation site of Cape Grim (CGO), Tasmania is well-suited for tracking even small changes in global background. Its continuous CF_4 observations (2006-2018) complemented by bottom-up data of national inventories and UNFCCC reports served as input data in a study of *Dunse et al. (2020)* comparing Australian and global emissions. Using the *NAME transport model* and the *InTEM inversion model* (Inversion Technique for Emission Modelling) Australian PFC emissions reveal a general decrease over time and were determined to make up 0.6% of global emissions in 2018 which were exclusively attributed to the aluminum industry (Dunse et al., 2020). A study by *Say et al. (2021)* used atmospheric measurements from five different AGAGE background sites (MHD, THD, RPB, SMO and CGO) and the *AGAGE 12-box model* to update global baseline growth rates from 2005-2019 through Bayesian

inversion. Measurements at MHD and three additional high-frequency observation sites in Northwest Europe (TAC, JFJ, CMN) served for estimated spatial emission distributions in this region derived with the *dispersion model NAME* in combination with the *InTEM inversion model*. Northwest European emissions were found to make up 0.7% of global emissions in 2018 (Say et al., 2021). Building up on their work, the latest study by *Guo et.al. (2024)* uses atmospheric measurements of the *US National Oceanographic and Atmospheric Administration (NOAA)*, the *Advanced Global Atmospheric Gases Experiment (AGAGE)*, and the *National Institute for Environmental Studies (NIES)* in combination with atmospheric transport model FLEXPART to further refine global CF_4 emissions (Guo & Fang, 2024).

With the introduction of international and national policy frameworks, research on CF_4 as a potent GHG has slowly gained more attention. While its emission estimations have improved over time especially by increasing numbers of measurements and efforts on improved emission factor calculations, most studies keep stressing persistent discrepancies between reported and measured concentrations highlighting the need for a higher density of global monitoring sites for verification. While East Asia and China in particular has been identified to be a major contributor to global CF_4 emissions, global spatial emission distributions including other high emitting regions have been studied less, since it requires globally distributed measurements, regionally resolved a priori emission estimates and well-performing transport and inversion models with high computing capacities. With latest improvements and extensions, the FLEXPART modeling family appears to be an appropriate choice for such a global top-down inversion that might fill gaps in regional and global emission estimates.

2. Inverse Modeling Principles and the FLEXPART Family: A Top-Down Approach to Emission Estimation

In the case of top-down GHG emission estimation inverse modeling relies on four types of input data that have to be gathered before performing the actual inversion: Prior emission estimates (a priori emissions), observational data and corresponding emission sensitivities of the observation sites (source-receptor relationships) as well as background concentrations. The following section explains the input data and principles to prepare and perform an inversion using the FLEXPART family.

2.1. Primary Constraint – A Priori Emissions and Observations

As inverse modeling is an optimization process, a priori emission estimates serve as primary emission constraint. Otherwise the inversion would be ill-conditioned and may lead to spurious emission esti-

mates, especially in regions not well covered by the observation network (Tarantola, 2005). Prior emissions are obtained from bottom-up inventories and usually rely on previous studies, sectoral activity data, emission factors, or national and global reports. Observational data measuring atmospheric trace gas concentrations at multiple observation sites (receptors) further constrain the inversion to optimize the prior estimates. Observation sites can either be ground-based monitoring stations with automated continuous or flask-based sampling, moving platforms like aircraft, ship or balloon campaigns that mostly use a flask-based approach and for some cases even satellites that use remote sensing (Dutton et al., 2017; NASA, 2024). Their spatio-temporal resolution and coverage directly influence the accuracy of emission estimates obtained by the inversion (a posteriori emissions) (Tarantola, 2005). Uncertainty estimates influence the balance between observational and prior emission constraints in the a posteriori emissions (Tarantola, 2005).

2.2. Determination of Source-Receptor-Relationships with FLEXPART

In order to link measured concentrations observed at receptors to their emission sources within the receptor-surrounding source area, inverse modeling also requires prior information from atmospheric transport models that calculate so-called source–receptor relationships (SRRs) (Clappier et al., 2015; Seibert & Frank, 2004). Before the introduction of backward modeling in Lagrangian Particle Dispersion Models (LPDMs) like FLEXPART, SRRs were estimated using forward dispersion simulations, adjoint models, statistical methods or grid-based Eulerian backward models. Forward models released particles from known sources tracking their dispersion, which was computationally expensive and less effective for unknown sources (S. Li & Du, 2020). Adjoint mathematical models solved the reverse transport equation numerically but faced similar challenges with computational cost and were complex to implement (Gandarillas et al., 2024), while Eulerian grid models struggle with limited spatial accuracy in long-range transport due to numerical problems (Stohl et al., 2004). The *NAME model*, used in several recent studies such as *Arnold et al. (2018), Say et al. (2021),* and *An et al. (2024),* is a Lagrangian Particle Dispersion Model (LPDM) developed by the UK Met Office. While NAME is capable of simulating long-range atmospheric transport, it has been primarily applied in regional and continental-scale studies (Jones et al., 2007). In contrast, FLEXPART is more commonly used for global-scale applications, offering greater flexibility in handling various meteorological datasets (e.g., ECMWF, GFS) and better computational efficiency for long-range backward simulations (Pisso et al., 2019). FLEXPART's ability to simulate atmospheric transport over several weeks or months with large particle ensembles makes it particularly well suited for inverse modeling of long-lived trace gases on global scales. Backward modeling with LPDMs like FLEXPART and NAME enables efficient identification of source-receptor relationships by tracking particles from observation sites to source regions, avoiding the high computational demands of full-domain Eulerian simulations (Stohl et al., 2004).

FLEXPART is a *Lagrangian Particle Dispersion Model (LPDM)*, a stochastic modeling approach introduced by *Thomson et. al. (1987)* simulating atmospheric transport by calculating particle trajectories (Thomson, 1987). Each simulated particle represents a parcel of tracer material moving according to the ambient flow conditions considering advection by mean flow, turbulent diffusion, and deposition or chemical reactions. It uses meteorological fields as input from datasets such as the *European Centre for Medium-Range Weather Forecasts (ECMWF)* or the *Global Forecast System (GFS)* (Pisso et al., 2019). In its backward mode FLEXPART can trace the history of particles moving backwards in time and space from a given receptor location like a measurement station to determine the source regions that contributed to observed concentrations. The modeled domain is thereby divided into spatio-temporal grid cells in which the resulting source-receptor relationships quantify the link between measured changes in concentrations at a receptor and the corresponding surface fluxes (emissions) from surrounding sources (Pisso et al., 2019). Mathematically, the SRR between a receptor and an emission source in a given spatio-temporal grid cell *(i, n)* is represented as the average residence time of *J* back-trajectories (particle releases) within that cell:

$$\partial y \Big/ \partial x_{i,n} = \frac{1}{J} \sum_{j=1}^{J} \frac{\Delta t'_{i,j,n}}{\rho_{j,n}} \quad (1)$$

where $\Delta t_{i,j,n}$ is the residence time of trajectory j in the spatio-temporal grid cell *(i, n)* and $\rho_{j,n}$ is the air density in the grid cell (Seibert & Frank, 2004; Thompson & Stohl, 2014). This equation essentially describes the sensitivity of a receptor to flux changes in the surrounding spatio-temporal grid cells as the total average residence time of air parcels in a given grid cell weighted by air volume per unit mass (air density). This allows measured concentration changes at a receptor to be mathematically related to surface fluxes (emissions) measured in mass per unit area per unit time enabling the scaling of flux contributions and the estimation of concentration contributions by inverse modeling (Thompson & Stohl, 2014). For CF_4, atmospheric loss processes can be neglected as it has no significant sinks on timescales of SRR calculations, making this method suitable to calculate SRRs on long-range scales.

Continuous improvements over the last two decades, for instance in terms of meteorological data input, performance, physicochemical parameterizations, input and output formats, and available preprocessing and post-processing options, have made FLEXPART a widely used, well-performing model. Furthermore, its parallel efficiency greater than 75 % significantly reduces computational costs through parallel computing strategies, such as particle splitting techniques that distribute computational workload across

multiple processors (Pisso et al., 2019). This makes it possible to perform backward runs over longer time periods up to months, which increases the sensitivity to emissions, especially in regions not well covered by the measurement network.

2.3. Atmospheric Background Concentrations

At the endpoints of the transport model's back trajectories defining the boundaries of the inversion domain, background concentration fields are applied to introduce the initial atmospheric composition. These fields serve as a baseline against which enhancements from regional emissions are identified and quantified (Tarantola, 2005). For long-lived species like CF_4 most of the short-term variability in concentration changes measured at a receptor is caused by emissions from close by spatio-temporal grid cells within the last few days before a measurement (Pisso et al., 2019). This information is significant to estimate the spatial emission distribution. The low-variable long - term trend however dominates measured concentration and represents the total CF_4 accumulation of past global emissions. Since emissions slowly lose information on their spatio-temporal origin as they become more and more dispersed, earlier or far away emission events are mostly smoothed out by atmospheric mixing contributing to a growing global background concentration. Accordingly, when measuring atmospheric CF_4 concentrations the background concentration is the dominant fraction of the total concentration (Pisso et al., 2019). By separating the background component from the informative short-term fluctuations, inverse modeling approaches can reveal these recent emission contributions in the source area of a receptor, with SRRs quantifying the contributions from specific areas or sources (Pisso et al., 2019). Thus, it is necessary to calculate the background contribution as an initial starting concentration before the simulation determines the additional short-term emissions within the inversion period. A recent study by *Vojta et. al (2022)* compared different methods of background calculations and suggested a global-distribution-based (GDB) method where a global field of mixing ratios is multiplied with the source-receptor sensitivities at the termination point of the back trajectories (Vojta et al., 2022).

2.4. Baseline Determination with FLEXPART LCM (Lagrangian Chemical Model)

The global background concentration fields can be determined by Lagrangian chemical transport models such as FLEXPART CTM (Chemical Transport Model) or FLEXPART LCM respectively (Groot Zwaaftink et al., 2018; Pisso et al., 2019) or by Eulerian chemistry transport models.

FLEXPART LCM (Linear Chemistry Module) is an extension to FLEXPART-CTM which was developed to perform mass-based global domain filling simulations of tracer species yielding concentration

fields. These tracers are represented by particles with assigned molar masses to track concentration fields while accounting for chemical transformations and loss processes along atmospheric transport. Each parcel represents a fraction of the total atmospheric mass according to its atmospheric mixing ratio (concentration). The LCM module enables the initialization of particle mass from pre-defined concentration fields such as latitude profiles, while a priori emission data are used during the simulation to adjust the particles' initial mass according to surface flux (emission) input along its transport. Optionally, chemical transformation processes can be included (Groot Zwaaftink et al., 2018). To account for model error and biases in the input emission fields, observational constraints are incorporated using a nudging technique, where model values are relaxed towards measurements within predefined spatio-temporal kernels around the observation location and time (Vojta et al., 2022).

FLEXPART-CTM is based on FLEXPART 8 (Henne et al., 2018) operating in domain-filling mode. With particles being continuously transported across the entire model domain representing overall atmospheric background conditions, it finally estimates concentrations at receptor points using a kernel method. Since particles fill the entire domain, every grid cell has tracer mass information. The receptor kernel additionally weights nearby particles for kernel-based smoothing of the final concentration at receptors (Henne et al., 2018).

The concentration at a receptor location is calculated as:

$$c_s(x,y,z) = \sum_{i=1}^{N} \frac{m_{s,i}}{h_{x,i} h_{y,i} h_{z,i}} K(r_x, r_y, r_z)$$

(2)

where *x, y, z* are the coordinates of the receptor, h_x, h_y, h_z are kernel widths in each dimension and r_x, r_y, r_z are the normalized particle-receptor distances

$$r_x = \frac{(X_i - x)}{h_{x,i}}, r_y = \frac{(Y_i - y)}{h_{y,i}}, r_z = \frac{(Z_i - z)}{h_{z,i}}$$

(3)

with *X, Y, Z* being the coordinates of an individual particle. $K(r_x, r_y, r_z)$ is the Kernel function with the volume integral $I = 1$ and $f = 2$ for receptors at the model surface (Henne et al., 2018).

$$K(r_x, r_y, r_z) = f\frac{15}{8\pi}(1-r^2)I,\ I = \begin{cases} 1 \text{ for } r^2 = r_x^2 + r_y^2 + r_z^2 < 1 \\ 0 \text{ otherwise} \end{cases}$$

(4)

For each particle-observation pair the temporal kernel weight, w_t and the spatial kernel weight, w_s are calculated as:

$$w_{t,kl} = \left(1 - \left|\frac{t_k - t_l}{h_t}\right|^3\right)^3$$

(5)

$$w_{s,ij} = f_s(1 - r_{ij}^2)I,\ I = \begin{cases} 1 \text{ for } r^2 < 1 \\ 0 \text{ otherwise} \end{cases}$$

(6)

where h_t is the temporal kernel width, t_k the current model time and t_l the time of the closest valid observation and the spatial kernel extent r_{ij} (h_x,h_y,h_z) being calculated as

$$r_{ij}^2 = \left(\frac{X_j - x_i}{h_{x,j}}\right)^2 + \left(\frac{Y_j - y_i}{h_{y,j}}\right)^2 + \left(\frac{Z_j - z_i}{h_{z,j}}\right)^2$$

(7)

The resulting nudging tendency $\Delta m_{n,i}$ for a particle is obtained by (Henne et al., 2018)

$$\Delta m_{n,i} = w_{s,ij} w_{t,kl} \frac{M_{j,l} - m_i}{\tau_n} \Delta t$$

(8)

Using a smaller kernel can better capture variability of near surface receptors which are more sensitive to small spatial differences whereas larger kernels are used for receptors at higher altitudes or in regions

with less spatial variability (Vojta et al., 2022). This routine ensures that the simulated tracer parcels better align with actual observed data and reduces model bias. Comparing the modeled output concentrations with real observations at a receptor reveals the model's performance and bias. The concentration output of LCM provides gridded information of background concentration for the whole globe and at any given time point and thereby provides the initial background concentration at the starting point of an inversion. Accurate baseline concentrations are important in inverse modeling in that they directly influence the accuracy of emission estimates itself.

2.5. Inverse Modeling with FLEXINVERT+

Inverse modeling is finally applied to optimize the prior emission fields and obtain a refined estimation of short-term emission fluxes within a specified area and period. A suitable starting point for an inversion can be determined by finding a time point of homogenous SRR distribution within the chosen inversion area. The relationship between emissions and measured observations is given by the transport matrix operator within a forward model (Thompson & Stohl, 2014):

$$y = Hx \tag{9}$$

where y represents the observed concentrations at receptor locations, x denotes the state vector constructed from emissions plus the background, and H is the transport operator. This equation serves as the basis for the inverse approach, where the goal is to estimate x from the known observations y and sensitivity information H constructed from the two components H^{mod} and H^{bg} in the case of a global inversion. The SRR input provides continuous information about the sensitivity operator H^{mod}, which represents the contribution of fluxes within the inversion period, as well as the initial sensitivity operator H^{bg} representing the contribution of initial mixing ratios at the starting point of the inversion (Thompson & Stohl, 2014). The inversion uses the initial sensitivity H^{bg} together with the initial concentration input y^{bg} of FLEXPART-CTM and can in fact also optimize the background. This further extends Equation 10 to:

$$y = Hx = H^{mod} f^{mod} + H^{bg} y^{bg} \tag{10}$$

Where H^{mod} and H^{bg} are the sensitivity operators, f^{mod} are the fluxes within the inversion period and y^{bg} is the initial concentration (Thompson & Stohl, 2014).

Inverse modeling essentially solves its optimization problem by adding information from observations (y) and SRR sensitivities (H) to the prior estimates (x_p) to finally obtain the optimized posterior state (x), where K is the gain matrix determining the influence of observational data.

$$x = x_p + K\,(y - Hx_p) \tag{11}$$

Based on the match between prior (Hx_p) and observed (y) mixing ratios, FLEXINVERT+ reconstructs the most likely emission sources contributing to the observed concentrations. Mathematically, this optimization is solved according to Bayes' theorem by minimizing the difference between posterior and prior state (x - x_p) as well as between modelled and observed mixing ratios (Hx - y). This, in total, minimizes the cost function to ensure the optimal balance between observational constraints and prior estimates while accounting for uncertainties in both emissions and observations under the assumption of Gaussian distribution (Thompson & Stohl, 2014).

$$J(x) = \frac{1}{2}\left(x - x_p\right)^T B^{-1}\left(x - x_p\right) + \frac{1}{2}\,(Hx - y)^T R^{-1}(Hx - y) \tag{12}$$

where B is the prior error covariance matrix which determines the influence of the prior state x_p and R is the observation error covariance matrix that weighs the influence of observations y. As the inversion progresses, the model gradually assigns more weight to recent emissions as SRRs become increasingly localized in time and space. This leads to a spatially and temporally resolved reconstruction of emission sources, including contributions from previously unidentified regions.

2.6. Errors and Uncertainties of the FLEXINVERT+ Inversion

The model's output, however, comes with a total uncertainty, which is continuously accounted for during the inversion by considering correlated errors. The prior error covariance matrix *B* determines the confidence in prior flux estimates and correlates these flux errors over space and time during the inversion. These errors originate from uncertainties in emission inventories, emission factors, upscaling, or modelling. As an estimation, spatial and temporal flux correlations are assumed to follow exponential decay resulting in the combined spatiotemporal correlation matrix. If *B* is set high, it means the prior fluxes are less reliable, allowing the inversion to make larger adjustments based on observations, while a lower *B* places more trust in prior flux estimates limiting adjustments during inversion (Thompson & Stohl, 2014). Similarly, the observation error covariance matrix *R* indicates the trust in observation constraints and accounts for errors in measurements, transport, and representation. *R* uses a diagonal matrix of the three errors' quadratic sum as an estimated correlation pattern. A high *R* reflects a higher uncertainty in observations allowing the inversion to rely more on prior estimates. Conversely, a low *R* gives more weight to observations (Thompson & Stohl, 2014).

During the inversion the prior error covariance matrix *B* is combined with the observation error covariance matrix *R* to calculate the gain matrix *K* determining the influence of prior emission estimates and observational data. The inversion continuously updates the flux estimates (x) by using the gain matrix *K* to adjust the prior fluxes (x_p) refining their values based on observational constraints (y) (see Equation 13). A higher *K* gives more weight to observations, whereas a lower *K* implies that prior emission estimates remain more dominant. For the case where the number of observations (y) is smaller than the number of prior state variables (x_p) *K* is determined as (Thompson & Stohl, 2014)

$$K = BH^T(HBH^T + R)^{-1} \quad (13)$$

After the inversion the posterior error covariance matrix *A* can be computed from *B, R,* and *K* to obtain the updated posterior uncertainty of the posterior flux estimates (x) to be compared to *B* and reveal the reduction from the prior uncertainty (Thompson & Stohl, 2014)

$$A = B - KHB \quad (14)$$

A lower A indicates that the inversion has reduced uncertainty, meaning that the modeled posterior fluxes are more confident compared to prior flux estimates. A high A on the other hand means that the inversion could not refine prior estimates significantly. This is the case for regions with high prior uncertainty and / or low observation density.

3. Input Data and Model Setup for Global CF_4 Emission Estimations with FLEXINVERT+

In this study we perform a global inversion using FLEXINVERT+ over a 100-day period to quantify CF_4 emissions and analyze their spatio-temporal distribution from 2006 to 2023. We expect our top-down approach to provide more accurate and spatially refined emission estimates compared to existing global bottom-up data. This assumed improvement is based on improved bottom-up prior emission estimates scaled to global top-down values, the integration of all available observational data, particularly new data from China and the U.S., the enhanced computational efficiency of our atmospheric transport model FLEXPART for spatiotemporally resolved long-range transport simulations, the use of the advantageous GDB method for baseline calculations, and the application of a Bayesian inversion framework. With our modelling approach we aim to identify emission hotspots, highlight discrepancies with bottom-up inventories, and improve accuracy particularly in areas where the measurement network is relatively dense. The prior emission estimates, observational data, and the model setup are explained in detail in the section 3. including the configuration of FLEXPART and its extensions FLEXPART-CTM and LCM as well as FLEXINVERT+.

3.1. A Priori Emission Data

All prior emission estimates used in our inversion are based on the spatially resolved *Emissions Database for Global Atmospheric Research (EDGAR) version 8.0* (European Commission & Joint Research Centre (JRC), 2023) as it is the only available gridded bottom-up emission inventory for CF_4. To estimate GHG emissions, EDGAR consistently uses a technology based emission factor approach for all countries that sums up the country-specific emission contributions of all sectors, technologies and abatement measures. The relative contributions are estimated by factors for human activity data, the mix of technology, the effectiveness of abatement measures, and the country-specific emission factor, obtained primarily from country reporting. If country reports are not available EDGAR F-Gas estimates are based on international statistics, data from the *United Nations Environment Program (UNEP)*, scientific literature, and expert judgment (Janssens-Maenhout et al., 2019). Yearly estimates are temporally scaled to

a monthly resolution using sector- and region-specific monthly profiles and spatially provided as high-resolution gridded data (0.1° x 0.1°) based on spatial distribution information about energy and manufacturing facilities, road networks, shipping routes, human and animal population density as well as agricultural land use (Janssens-Maenhout et al., 2019).

Other databases of bottom-up emission estimations, such as the *Greenhouse Gas Initiative Scenario Database (GGIDB)* (International Institute for Applied System Analysis (IIASA), 2009), often only provide total PFC emission estimations or estimates on a yearly or global total resolution, making these bottom-up databases unsuitable for spatio-temporally resolved emission estimates of CF_4 only. Comparing the global sum of EDGAR data with that of bottom-up reports of the *UNFCCC Greenhouse Gas Inventory* (United Nations Framework Convention on Climate Change (UNFCCC), 2024) reveals drastic discrepancies typically by factors of 2 - 10, which can be even higher on country-level. Therefore, we adjusted the EDGAR prior in regions where such mismatches were especially

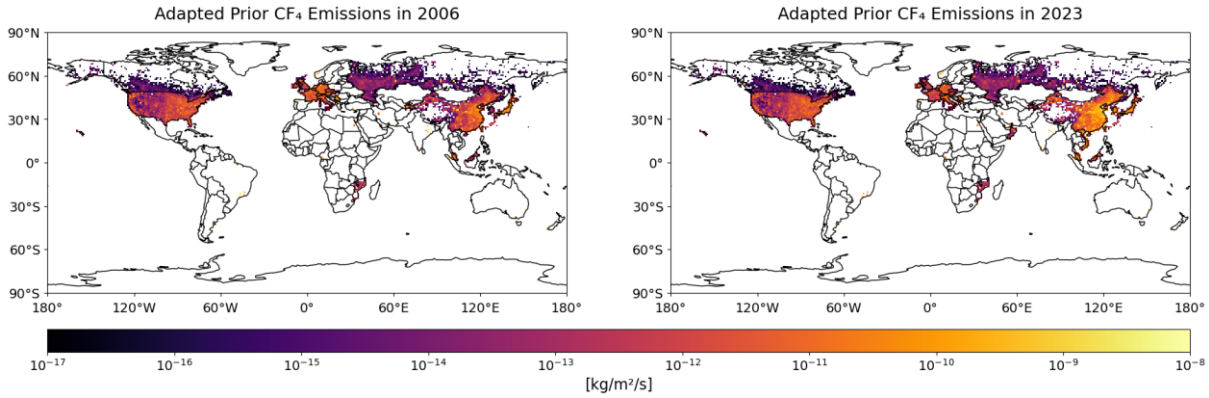

Figure 1: The spatial distribution of prior emissions in 2006 and 2023 over the whole globe reveals a global increase in emissions from the first (2006) to the last (2023) year of our studied period and hints to potential major contributors, like China, Russia, Europe and the U.S. Distribution patterns and magnitudes, that are ranging from 10^{-17} kg/m²/s (dark blue) to 10^{-8} kg/m²/s (light yellow) are based on data from the Emissions Database for Global Atmospheric Research (EDGAR) version 8.0 (European Commission & Joint Research Centre (JRC), 2023) with quantitative adaptions in China and India.

pronounced, based on the method of *Püschel (2025),* who performed test runs of different prior settings for the PFC C_2F_6, which is comparable to the case of CF_4: For China, we incorporated regional, industry-based bottom-up estimates from *Guo et al. (2023)*, which align with recent top-down studies by *Kim et al. (2021)* and *An et al. (2024)*, and scaled the national average to the EDGAR spatial distribution. In the case of India, prior emissions were adapted by averaging EDGAR values with a yearly extrapolation of the 2020 estimate from *India's Fourth Biennial Update Report to the UNFCCC*, based on primary aluminum production data (Ministry of Environment, Forest and Climate Change (MoEFCC), 2024; Püschel, 2025). Both, the EDGAR as well as most of the UNFCCC data do not report uncertainty ranges. However, given that discrepancies in the two bottom-up inventories reach factors of up to 500 in some years or regions, we assume a 100% uncertainty for all our priors (see section 3.5.). Figure 1 compares

the spatial distribution of our prior emission estimates from the first (2006) and the last (2023) year of our studied period resembling an estimated global increase of ~67% and hinting to potential major contributors, like China, Russia, Europe and the U.S..

3.2. Observational Data

SITE ID	*STATION NAME*	*MEASUREMENT TYPE*	*START - END YEAR*	*COORDINATES (LAT, LON)*	*COUNTRY*
thd	Trinidad Head	Continuous, Flask	2005 - 2023	(41.05, -124.15)	United States
cgo	Cape Grim, Tasmania	Continuous, Flask	2005 - 2023	(-40.68, 144.69)	Australia
mhd	Mace Head	Continuous, Flask	2005 - 2023	(53.33, -9.9)	Ireland
rpb	Ragged Point, Barbados	Continuous	2005 - 2023	(13.17, -59.43)	Barbados
smo	Cape Matatula, American Samoa	Continuous, Flask	2006 - 2023	(-14.25, -170.56)	United States
gsn	Gosan	Continuous	2007 - 2019	(33.29, 126.16)	South Korea
jfj	Jungfraujoch	Continuous	2010 - 2023	(46.55, 7.99)	Switzerland
sdz	Shangdianzi	Continuous, Flask	2010 - 2021	(40.65, 117.12)	China
tac	Tacolneston	Continuous	2012 - 2023	(52.52, 1.14)	United Kingdom
wlg	Mt. Waliguan	Flask	2012 - 2021	(36.29, 100.9)	China
lan	Lin'an	Flask	2012 - 2021	(30.3, 119.73)	China
lfs	Longfengshan	Flask	2012 - 2021	(44.73, 127.6)	China
xgl	Shangri-La	Flask	2012 - 2021	(28.01, 99.44)	China
brw	Barrow	Flask	2014 - 2021	(71.32, -156.61)	United States
mlo	Mauna Loa	Flask	2014 - 2022	(19.54, -155.58)	United States
lef	Park Falls, Wisconsin	Flask	2014 - 2022	(45.95, -90.27)	United States
sum	Summit	Flask	2014 - 2021	(72.58, -38.46)	Greenland
spo	South Pole	Flask	2014 - 2021	(-89.98, -24.8)	Antarctica
nwr	Niwot Ridge	Flask	2014 - 2022	(40.05, -105.59)	United States
alt	Alert	Flask	2014 - 2021	(82.5, -62.3)	Canada
psa	Palmer Station	Flask	2014 - 2021	(-64.77, -64.05)	Antarctica
zep	Zeppelin	Continuous	2014 - 2023	(78.91, 11.89)	Norway
kum	Cape Kumukahi	Flask	2014 - 2021	(19.52, -154.81)	United States
hfm	Harvard Forest, Massachusetts	Flask	2014 - 2021	(42.54, -72.17)	United States
trl	Trollhaugen	Continuous	2015 - 2024	(-72.01, 2.54)	Antarctica
mbo	Mt. Bachelor Observatory	Flask	2016 - 2021	(43.98, -121.69)	United States
mrc	Marcellus Pennsylvania	Flask	2016 - 2021	(41.47, -76.42)	United States
wkt	Moody, Texas	Flask	2016 - 2021	(31.31, -97.33)	United States
wbi	West Branch, Iowa	Flask	2016 - 2021	(41.72, -91.35)	United States
crv	Carbon in Arctic Reservoirs Vulnerability Experiment (CARVE)	Flask	2016 - 2021	(64.99, -147.6)	United States
wgc	Walnut Grove, California	Flask	2016 - 2021	(38.26, -121.49)	United States
amt	Argyle, Maine	Flask	2016 - 2021	(45.03, -68.68)	United States
str	Sutro Tower, San Francisco	Flask	2016 - 2021	(37.76, -122.45)	United States
mwo	Mt. Wilson Observatory	Flask	2016 - 2021	(34.22, -118.06)	United States

msh	Mashpee, Massachusetts	Flask	2016 - 2021	(41.66, -70.5)	United States
lew	Lewisburg, Pennsylvania	Flask	2016 - 2021	(40.94, -76.88)	United States
lac	LA Megacities	Flask	2017 - 2021	(33.88, -117.88)	United States
sct	Beech Island, South Carolina	Flask	2017 - 2021	(33.41, -81.83)	United States
jgj	Jiangjin	Flask	2017 - 2021	(29.15, 106.15)	China
tmd	Thurmont, Maryland	Flask	2017 - 2021	(39.58, -77.49)	United States
akd	Akedala	Flask	2017 - 2021	(47.1, 87.93)	China
sgp	Southern Great Plains	Flask	2017 - 2021	(36.61, -97.49)	United States
nwb	NW Baltimore	Flask	2018 - 2021	(39.34, -76.69)	United States
xfg	Xinfeng	Flask	2018 - 2021	(24.08, 114.17)	China
amy	Anmyeon-do	Flask	2018 - 2021	(36.54, 126.33)	South Korea
neb	NE Baltimore, Maryland	Flask	2018 - 2021	(39.32, -76.58)	United States
bwd	Brentwood, Maryland	Flask	2019 - 2021	(38.93, -76.96)	United States
jsa	Jinsha	Flask	2019 - 2021	(29.64, 114.21)	China
cmn	Monte Cimone	Continuous	2022 - 2023	(44.19, 10.7)	Italy

Table 1: Overview on all observation sites used for the inversion including their site ID , name, measurement type, temporal activity and geographic location in coordinates as well as the country in which they are located. Observations start in 2005 and end in 2023 and are measured by a constantly increasing number of sites until 2021, when the number of observations sites with available data drops significantly. 12 out of 49 observation sites measure continuously while the rest are less frequent flask samples. An overview over the spatial distribution is given in Figure 2.

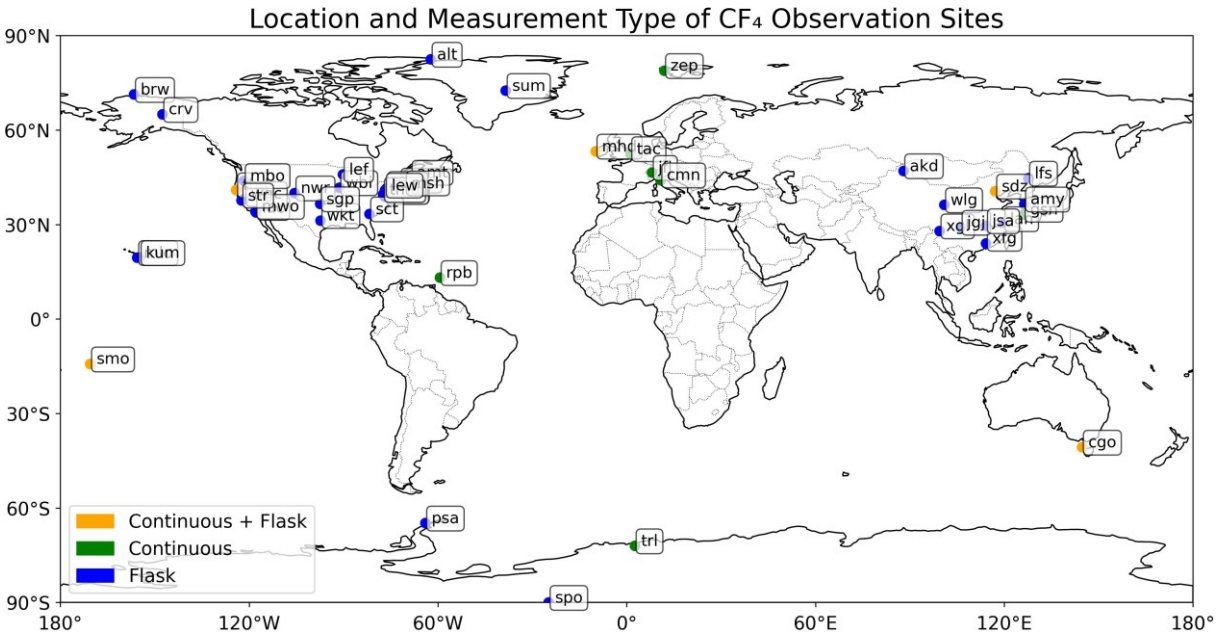

Figure 2: The spatial distribution of all observation sites included in our inversion reveals heterogenous patterns with clusters of observation sites in the Northern hemisphere, particularly in the U.S., East Asia, and North-West Europe, while the Southern Hemisphere is significantly less observed. Observation sites in less populated areas like Antarctica or within the Ocean are likely used to track background concentrations. Sites of in-situ continuous measurements are marked in green, flask measurement sites in blue and sites of both measurement types in orange. All data are provided by AGAGE (Advanced Global Atmospheric Gases Experiment) (Prinn et al., 2022), NOAA (National Oceanic and Atmospheric Administration) (Dutton et al., 2017) and the supplementary data published in the study of An et.al. (An et al., 2024). A more detailed overview is given in Table 1.

As observational input data we used CF_4 measurements available from 2006 until 2023 provided by *the Advanced Global Atmospheric Gases Experiment (AGAGE)* (Prinn et al., 2022), *the National Oceanic and Atmospheric Administration (NOAA)* (Dutton et al., 2017) and the supplementary data published in the study of *An et.al. (2024)*. All included observation sites, their name, location and temporal activity are given in Table 1. Introducing the *Medusa Gas Chromatography-Mass Spectrometry (GC-MS)* in 2006, AGAGE enabled the detection of very low concentrations for gases like CF_4 (Miller et al., 2008). The AGAGE high-frequency in situ measurement stations use an automated process that continuously samples air (every 2–4 hours) and concentrates the target gas in a cryogenic trap before passing it through the *Medusa GC-MS*. The data are stored digitally and shared through the AGAGE database (Prinn et al., 2022). Since the introduction of the *Perseus (PR1)* measurement instrument in 2014, NOAA provides CF_4 non-continuous but very accurate flask and aircraft measurement data. For our study we only used the flask measurements of NOAA collected automatically in stainless steel and/or glass flask pairs by the *HATS network*. The samples are then analyzed by GC-MS in NOAA's *Global Monitoring Laboratory* (Dutton et al., 2017). Before the start of in situ and flask measurements, concentration levels were only inferred from ice core and firn air archive and were not suitable for this research (Trudinger et al., 2016).

The temporal resolution of observations as well as the spatial coverage of observation sites is crucial in that it directly influences the inversion's performance and uncertainty minimization. Temporally, observation sites vary in their active measurement period as well as in their measurement frequency with continuous in-situ measurements generally providing a better temporal resolution than flask measurements. The global distribution of CF_4 measurement sites and their measurement type, plotted in Figure 2, highlights clusters of better observed regions like East-Asia, the U.S. and Central Europe, while major global regions like Russia, Central Asia, South America or Africa are not covered at

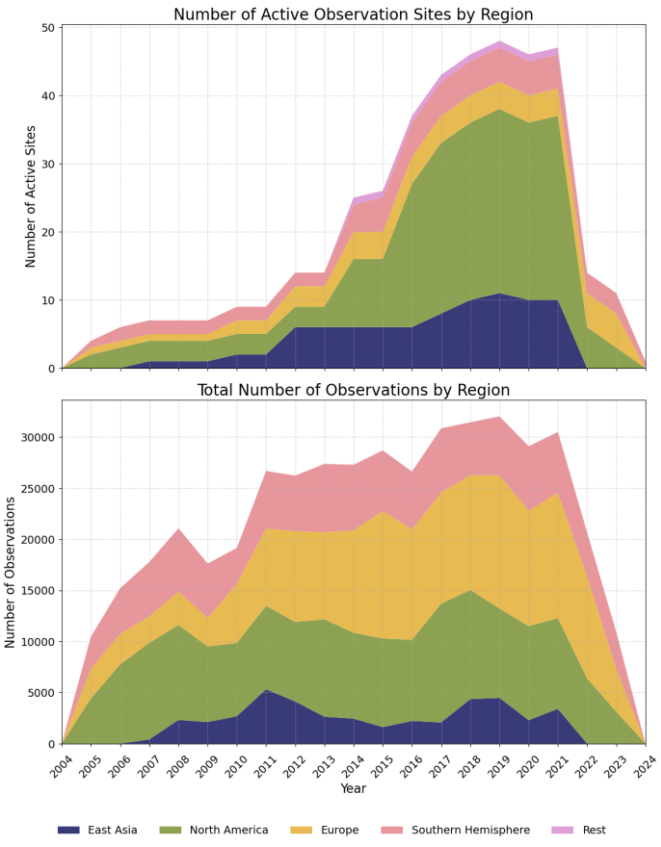

Figure 3: (Top) The number of active observation sites by region (East Asia in dark blue, North America in green, Europe in orange, the Southern hemisphere in coral and the rest in pink) shows a constant increase from no observation sites in 2004 to a peak of almost 50 in 2019. A particularly sharp increase starts in 2011with the addition of new sites in East Asia and in 2015 with the addition of observation sites in North America and East Asia. (Bottom) The total number of observations follows the overall rising trend until reaching a peak in 2019. In 2022 and 2023 the number of observation sites drops below 15 alongside with a significant drop in the total number of observations. North America and Europe contribute particularly high number of observations.

all, leading to a discrepancy in hemispheric coverage. Observation sites in Antarctica or on islands within the Ocean likely measure background concentrations, while stations close to populated and industry-rich areas likely track occurring emission events.

Figure 3 gives an overview over the number of active observation sites as well as the total number of observations within our studied period. This information is crucial for later interpretation of our inversion results in section 4. First observations started in 2005 with around 5000 measurements from four observation sites and already increased to more than 15.000 measurements in 2007. The total number of active measuring sites continuously rises until it reaches a peak of almost 50 active sites with more than 30.000 total observations in 2019 and does not drop significantly until 2021. Only in 2022 and 2023 the number of active sites dropped to less than 15 stations that still reported around 20.000 measurements in 2022, but only around 10.000 observations in 2023.

While North America, Europe and the Southern Hemisphere are covered by the observation network throughout the whole period, it is important to keep in mind that the whole region of East Asia was first covered with the start of measurements at Gosan in South Korea by the end of 2006 and intensified measurement frequency from 2008 on. Most notably, available measurements in East Asia stop at 2021 making the last two years, similar to the first year, of our studied period spatially significantly less constrained than the rest.

Nevertheless, specifically the inclusion of recently published new flask measurements from nine sites in China by *An et al.* (2024), as well as new flask measurements from the U.S. drastically increased the observational coverage in high emitting areas for some years. Together with two new continuous measurement sites in the Southern Hemisphere (TRL) and Europe (CMN), these data allow for improved spatio-temporally resolved emission estimates and have so far not been used in a global inversion.

Figure 4 shows the observation network as a punctual heatmap of mean observed concentrations within our studied period as well as the observed concentrations in specific regions. The measurements reveal similar patterns of emission distribution as the a priori data with notably high concentrations measured in East Asia that specifically increased from 2016 on and reached levels of more than 300 ppt. Significantly lower concentrations that rarely exceed 100 ppt were recorded in Europe and in the U.S. recorded concentration peaks start only in 2017 likely with the introduction of new measurement sites. Single peaks measured concentration often refer to single close-by emission events. All measurement data follow the same general slowly rising trend, which refers to the baseline that represents the globally distributed CF_4 background concentration. This trend seems to be well-tracked by measurements of the Southern Hemisphere, that are less influenced by single emission events. The calculated source-receptor-relationships discussed in the next section give a closer insight on the source area the observation network covers (see section 3.3.).

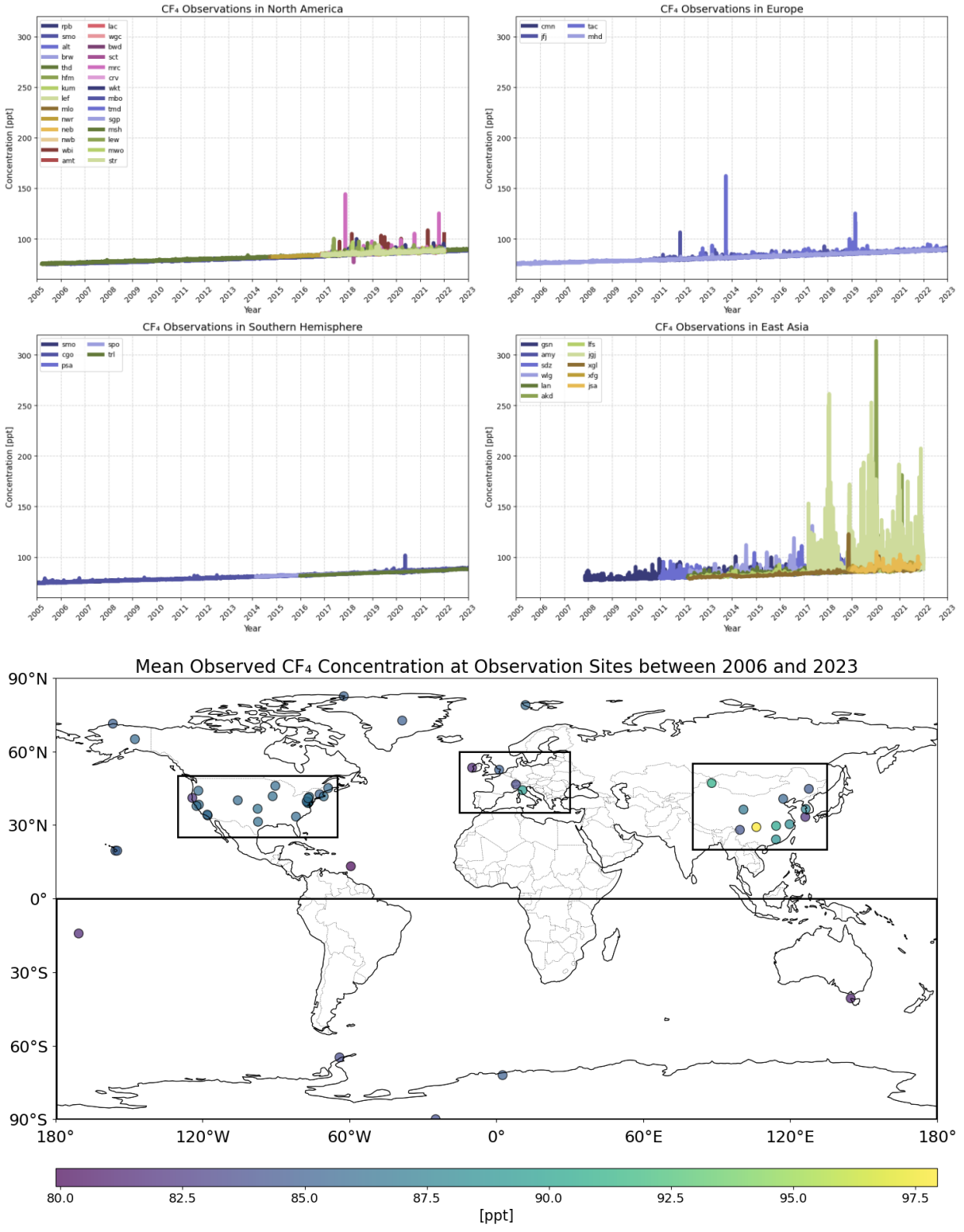

Figure 4: (Bottom) The map shows the locations of observation sites, colored by the mean total CF_4 concentration (in ppt) measured at each site. High-concentration sites like JGJ and AKD in China stand out in green-yellow, while lower than average background-level sites in purple, such as CGO and SMO, dominate the Southern Hemisphere. (Top) The line plots display concentrations (in ppt) from 2006 to 2023 at observation sites divided into four regions: North America, Europe, the Southern Hemisphere, and East Asia. The plots confirm the spatial patterns of the map, with East Asia showing particularly high concentrations. In contrast, the Southern Hemisphere largely reflects background levels. Europe and the U.S. record fewer and lower emission events than East Asia, though newer U.S. sites now capture some emission signals, whereas earlier data mostly reflect background conditions.

3.3. FLEXPART Configuration and Source-Receptor-Relationships

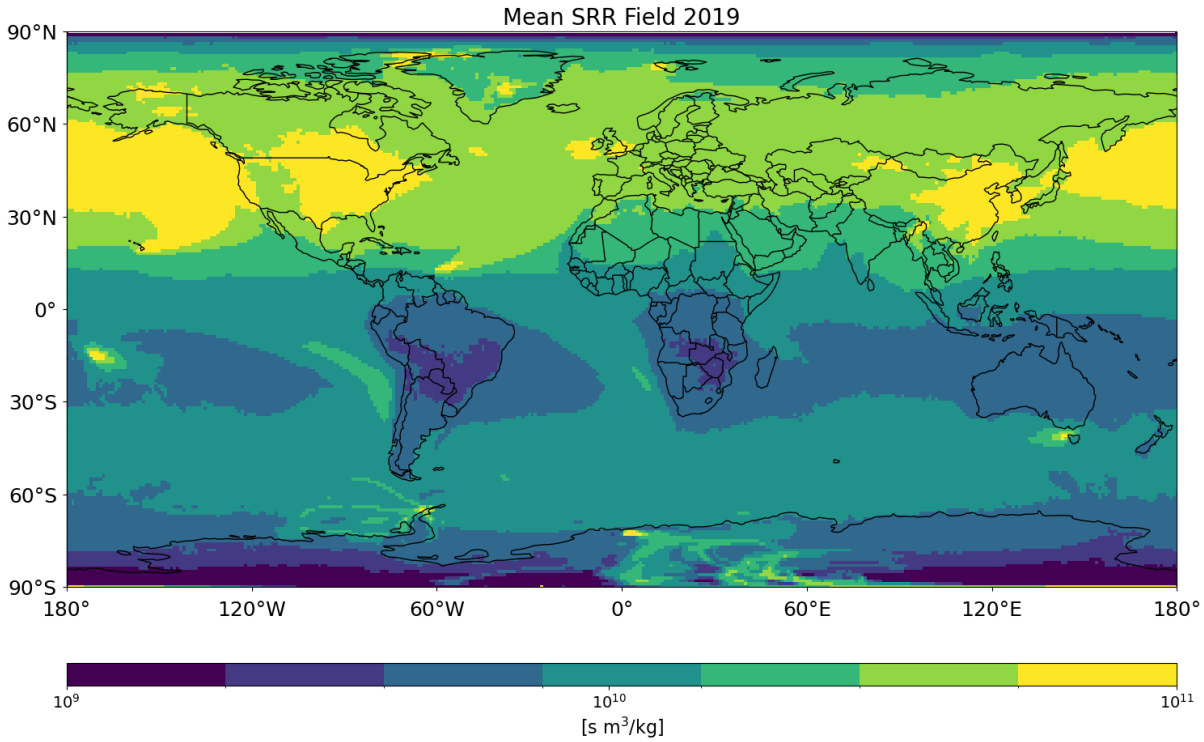

Figure 5: The mean source-receptor relationships in 2019 illustrate how well each region is covered by the sensitivities of the observation sites (receptors). Overall, the Northern Hemisphere is better covered than the Southern Hemisphere, with sensitivities ranging from 10^{10} to 10^{11} s·m³/kg, shown in mid-green to light green and yellow. The eastern U.S., eastern China, and the northern Pacific exhibit the highest coverage, followed by Europe, northern and central Asia, the Atlantic, and the rest of North America. In contrast, South America, Africa, Australia, the Arabian Peninsula, India, and South Asia are sparsely covered.

To calculate the SRRs relating emission fluxes to mixing ratios at measurement sites, in units of residence time × volume per mass (sm^3kg^{-1}) we used FLEXPART version 10.4 in backward mode (Pisso et al., 2019). 50,000 virtual particles were released per 3-hour averaging interval of measurements from the respective observation site (receptor) and traced backwards for 100 days using hourly ERA5 meteorological wind fields from ECMWF on a 0.5° x 0.5° horizontal resolution over 137 vertical levels (Hersbach et al., 2020). Due to computational limitations the backward simulation period is typically set to a few days to weeks only. Since our CF_4 observations are sparse and additionally averaged on 3h intervals, our computational capacities allowed for simulations over a comparably long time period, which was found to improve inversion accuracy compared to shorter simulation periods (Vojta et al., 2022). The resulting 1° x 1° output grid yields information on the time particles spend per day in each grid cell within the lowest 100 m above the surface where emissions are most likely to occur.

Figure 5 shows the mean SRRs for the year 2019, the year with the highest observation density, revealing the source areas covered by the transport model. Sensitivities are higher when closer to an observation

site and when measurements are sampled more frequently. The SRRs mainly match the expected pattern of observation network with a clear disbalance between sensitivities in the northern and the southern hemisphere. Northern latitudes between 40°N and 80°N are generally the best covered region. Especially, the East of China and the East of the U.S. as well as the U.S. west coast, the South of Canada, South Korea and the U.K. are well covered emission regions, while most background stations (e.g. CGO, RPB, or SPO) indeed exhibit high sensitivities over regions like the ocean or Antarctica. South America, Africa, India and the rest of South Asia, as well as Australia and northern Russia, exhibit low sensitivities, making these regions less constrained by observations and more dependent on prior emission estimates. The source-receptor relationships vary from year to year according to observation density.

3.4. FLEXPART LCM Configuration and Background Concentrations

3.4.1. Initialization with Latitudinal Profiles

To calculate the initial background concentration for our inversion we used FLEXPART (Version 11) with the *Linear Chemistry Module (LCM)* (Bakels et al., 2024) in forward domain-filling mode. To reduce computational cost the simulation was split into independent annual runs of the years 2006 – 2023 with 50 million particles released in each simulation. Instead of distributing particle mass uniformly over the entire globe, we used latitudinal profiles to ensure that particle mass was distributed in a way that reflects observed concentration gradients at different latitudes. The profiles were generated by averaging observed concentrations within a 60-day window prior to the start of each simulation. Depending on the availability of measurements in the respective time window the included observation sites can vary from year to year. An overview is given in Table 2. Stations that measure extremely high local emissions were generally excluded for the initialization of latitudinal background mixing ratios as they would have constrained the mixing ratios with recent emission events. Background stations like CGO, THD, SMO, MHD or RPB account for the general global background,

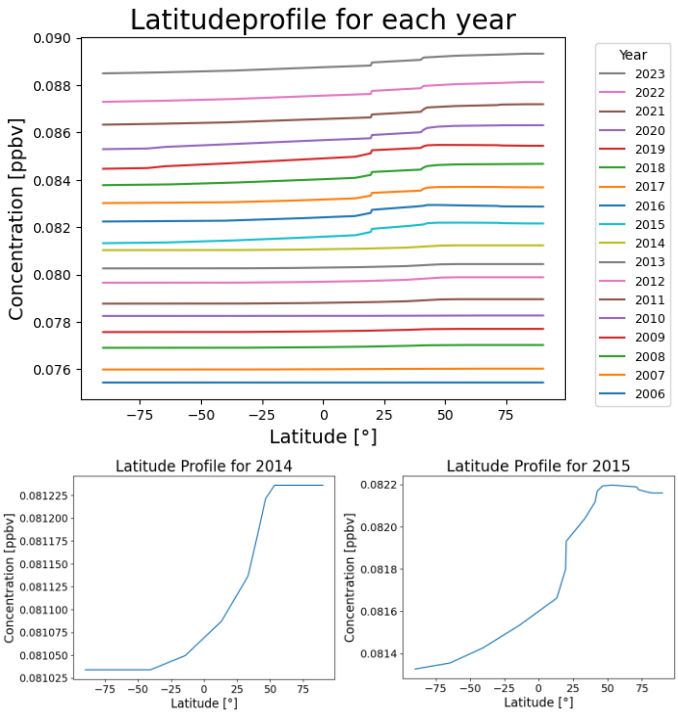

Figure 6: Latitude profiles for each year used to initialize the particle mass distribution across latitude bands based on observed gradients. North–South gradients are present in all years but become particularly pronounced from 2015 onward, when a significantly larger number of observation sites were included (see Table 2). From 2017 onward, an even more distinct gradient emerges, with pronounced peaks around 40°N.

while some northern hemispheric stations in high emission areas like GSN, JFJ, HFM or NWR account for the gradient in atmospheric mixing ratio between northern and southern hemisphere. Comparing the yearly latitude profiles (see Figure 6) reveals slight differences in the annual distribution of mixing ratios, which can be attributed to the respective observation sites included each year. For example, the inclusion of observations from several new sites in the Northern Hemisphere in 2015, compared to 2014, results in a more pronounced gradient between the Northern and Southern hemispheres. Additionally, we re-initialized every simulation year with a two-month spin-up period where initial concentrations given by the latitude profiles were nudged towards observations in order to reduce initial bias and computational costs and obtain a more realistic starting point for the actual simulation period.

Year	cgo	thd	mhd	rpb	smo	gsn	jfj	mlo	hfm	spo	brw	sum	kum	zep	psa	alt	nwr	trl
2006	X	X	X	X														
2007	X	X	X	X	X													
2008	X	X	X	X	X	X												
2009	X	X	X	X	X	X												
2010	X	X	X	X		X												
2011	X	X	X	X	X	X	X											
2012	X	X	X	X	X	X	X											
2013	X	X	X	X	X	X	X											
2014	X	X	X	X	X	X	X											
2015	X	X	X	X	X	X	X	X	X	X	X	X	X	X	X	X		
2016	X	X	X	X	X	X	X	X	X	X	X	X	X			X		
2017	X	X	X	X	X		X	X	X	X	X	X	X	X		X	X	
2018	X	X	X	X	X		X	X	X	X	X		X	X	X	X	X	
2019	X	X	X	X	X		X	X	X	X	X	X	X	X	X	X	X	X
2020	X	X	X		X		X	X	X	X	X	X	X	X	X	X	X	X
2021	X	X	X		X			X	X	X	X	X	X	X		X	X	X
2022	X	X	X		X			X		X	X		X	X		X	X	X
2023	X	X	X		X			X		X	X		X	X		X	X	X

Table 2: Observation sites included in the calculation of each annual latitudinal profile. GSN, JFJ, HFM and NWR are located close to industry areas, while the rest are located in areas far away from close by emission hotspots likely measuring background concentrations.

3.4.2. Nudging Impact and Global Baseline

In our simulation we produced daily concentration fields on a 3° x 2° output grid with 10 vertical levels (0.1 km, 0.5 km, 1 km, 3 km, 5 km, 7 km, 10 km, 15 km, 25 km, and 40 km above the ground) while accounting for emissions by adjusting the particles' mass when passing near emission sources. When particles are near measurement locations, simulated mixing ratios are nudged towards the measurements to reduce errors and biases and keep the model simulation close to the observations. The spatio-temporal

kernel sizes determine the nudging weight in space and time around each receptor explained in detail in section 2.4.

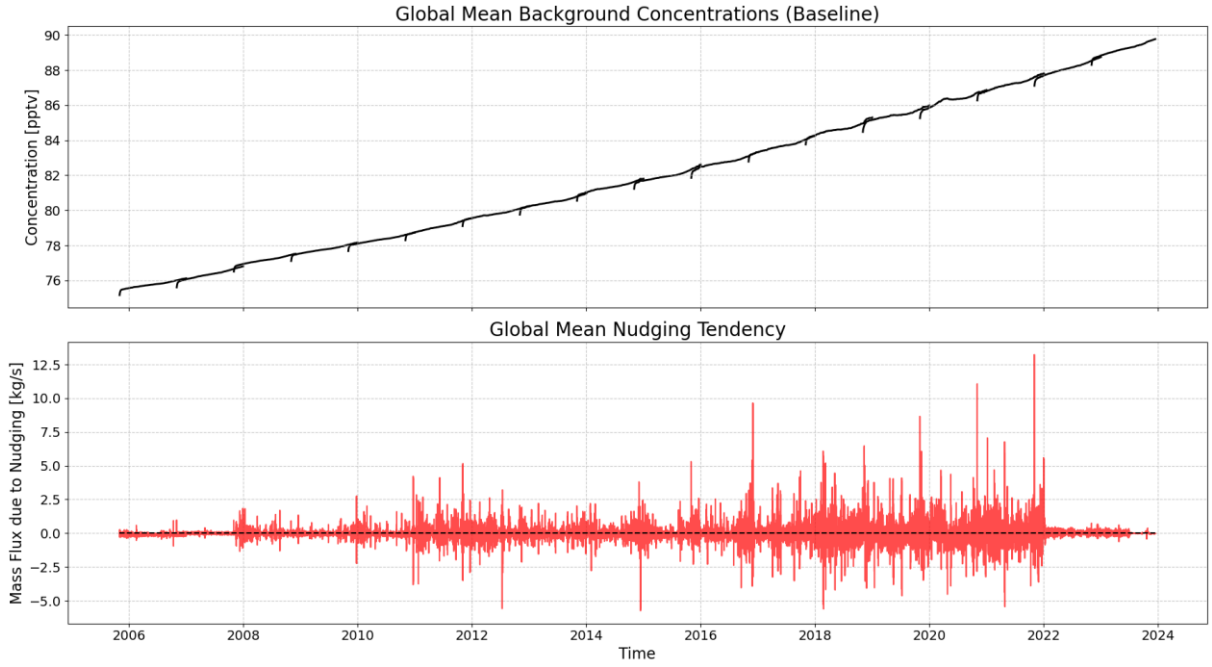

Figure 7: (Top) Global mean of all background concentrations (in pptv) obtained from independent annual LCM simulations over the whole study period. The annual simulations result in an overall mostly smooth baseline with overlapping two month spin-up phases in the beginning of each year. (Bottom) Nudging tendency expressed as mass flux (in kg/s) in the LCM simulation representing the adjustment of the simulated background concentrations towards observations. Positive values indicate an increase in particle mass to correct for concentrations that are too low, while negative values reflect a removal of mass to reduce concentrations that are too high.

We used horizontal kernel sizes ranging from 8° to 40°, a vertical kernel size of 1000 m, and a temporal kernel size of 10 days. The global mean concentration across all annual LCM simulations shows a rapid increase in concentration during the two-month spin-up period. This suggests that the initial mass distributed according to our latitude profiles was too low, likely because of the exclusion of some observation sites measuring higher-than-average concentrations and giving too much weight to background sites that tend to measure lower-than-average concentrations. However, after initialization nudging quickly adjusted the modeled LCM concentrations to align with all observations highlighting the impact of nudging on the particles' mass. Cutting out the two-month spin-up period, the global mean concentration remains relatively consistent and yields a smooth baseline (see Figure 7 (Top)). Figure 7 (Bottom) shows the global mean nudging tendency of all simulations. The overall increase over time reflects the growing need to adjust the model towards observations, likely because the growing number of observational sites, particularly near major emission regions, might track increasing discrepancies of the likely underestimated prior emissions that require larger corrections. With only five remote background stations initially, the nudging tendency remains low indicating that the model performs well in representing background concentrations at remote locations. A notable increase in nudging tendency follows the introduction of

Gosan measurement data, and later flask measurements from China and the U.S., which captured elevated concentrations from nearby emissions and led to upward adjustments of background concentrations. From 2016 onward, newly included high-concentration flask data further raise the nudging tendency, peaking during years with the highest observational coverage. A decline in nudging tendency after 2021 corresponds to a drop in observation data availability. While some observation sites capturing extreme local emission events were excluded to avoid overestimating the background, including measurements from high-emission regions is still important to ensure regional representativeness and prevent underestimation of background concentrations, particularly across the Northern Hemisphere. The resulting background fields are used as input for FLEXINVERT+ providing a baseline against which emission can be quantified. FLEXINVERT+ combines these global background fields with the SRR fields in the GDB background method to compute a weighted mean background concentration at each observation site and time.

3.5. FLEXINVERT+ Configuration

3.5.1. Spatio-Temporal Resolution

Our FLEXINVERT+ inversion was configured to estimate annual CF_4 emissions using a variable spatial grid (see Figure 8) for the emission field with spatial detail in well-constraint regions, coarser resolution in less constraint areas, and the exclusion of areas where no emissions were assumed (e.g. over oceans or antarctica). Breaking the inversion down to a yearly temporal resolution due to the annual nature of the a priori data and a variable spatial resolution strikes a balance between achieving well-resolved emission estimates while maintaining computational efficiency. This approach enables parallel processing and significantly reduces the number of state variables without compromising detail in key regions. The spatial grid is generated once based on SRRs and prior emission fields of 2019, as the year with the highest observational constraint, and applied uniformly across all years of the inversion. Starting with a coarse 8° × 8° resolution it becomes more resolved with 4° × 4°, 2° × 2°, or 1° × 1° grid cells in regions with strong prior emissions or observational constraint. To focus the analysis on plausible emission regions, all ocean and Antarctica grid cells were excluded from the

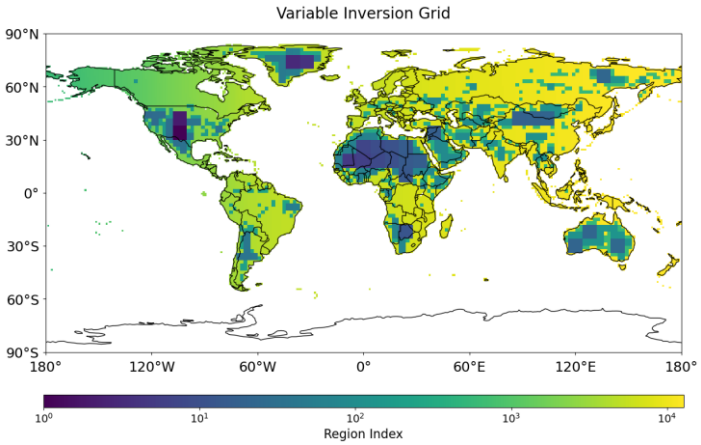

Figure 8: Spatial distribution of the variable-resolution region mask used in the inversion. Grid cells over the ocean and Antarctica are excluded and colored in white. The color bar indicates the region index, which categorizes grid cells based on spatial resolution.

inversion. In total this approach reduces the number of emission grid cells from 64,800 (on a uniform 1° × 1° grid) to just 7,789.

The 7,789 dimensions of the variable grid emissions together with 52 dimensions of the baseline result in 7,789 + 52 = 7,841 elements of the inversion state vector x for each year. The dimension of the observation vector y is determined by the total annual number of 3-hourly averaged measurements ranging from 7,096 to 17,698 entries depending on data availability for a given year.

3.5.2. Prior Error Covariance Matrix (B)

The prior error covariance matrix (B) accounts for uncertainties in prior emissions and the baseline along the diagonal and spatial and temporal correlations (Thompson & Stohl, 2014). After comparing our global total prior to global top down estimates of the *AGAGE 12-box model* by *Say et. al. (2021),* emission uncertainties were assumed to be 100% with a lower limit prior uncertainty of 1×10^{-14} kg/m²/h to avoid unrealistically small error values in low-emission regions. Baseline concentration uncertainties were fixed at 0.15 ppt and assumed to be uncorrelated as knowledge about long-range correlation structures is limited. Off-diagonal elements reflect spatial and temporal correlations in emission uncertainties, which were modeled using an exponential decay function with a 100 km spatial correlation length over land and a 90 day temporal correlation.

3.5.3. Observation Error Covariance Matrix (R)

The observation error covariance matrix (R) captures the total uncertainty of observations including the relatively small measurement error (typically around 0.05 ppt), the transport model uncertainty, and the representation error. Originating from multiple uncertainty factors in the transport model the dominant model transport uncertainty and representation error are practically difficult to quantify (Thompson & Stohl, 2014). To simplify these complex sources of error, a practical uncertainty scheme was applied based on methods used by *Henne et.al. (2016)* or *Vojta et al. (2024)*, where observed mixing ratios below 120 ppt were assigned a fixed uncertainty of 0.5 ppt, while for measurement values above this threshold the uncertainty was scaled linearly with the concentration. Based on our finding that the a priori modeled mixing ratios for CF_4 are relatively smooth compared to the highly variable observations near emission sources, we assumed that the model resolution may not fully capture this high variability and this approach accounts for increasing uncertainty for high concentrations. Lacking detailed information about observation dependencies the R matrix was treated as diagonal, assuming that measurement errors are independent and that no correlations exist between observations.

During the inversion, the entire state vector including emissions as well as background concentrations was optimized. Posterior emissions and their uncertainties were generated on a 1° × 1° grid as well as on the nested inversion grid.

3.6. Post-Processing Constraint and Regional Masks

To further constrain regions with weak observational coverage and optimize physically unrealistic or uncertain posterior values of the inversion an additional non-negativity constraint was applied to the inversion output based on the method of *Thacker (2007)* and implemented as:

$$x_c = x + AP^T(PAP^T + C)^{-1}(c - Px) \quad (15)$$

where x_c is the constrained posterior emission, x is the modelled posterior emission and A is the modelled posterior error covariance matrix (Thacker, 2007). In our inversion approach it is mathematically possible to obtain negative posterior emissions usually representing removal from the atmosphere into sinks. Since there are no sinks for CF_4 on the applied timescales, negative fluxes are physically unrealistic, which is why the non-negativity constraint sets any negative posterior emissions to zero following the method of *Thacker (2007)*.This is why c is a zero vector in this case with a zero uncertainty matrix C leaving the error covariance matrix A unchanged. P is a matrix with ones at the respective positions that correspond to negative posterior emission values in x (Püschel, 2025; Thacker, 2007).

For a detailed analysis at national and regional scales, we applied spatial masks according to country boundaries. This approach again follows the method used by *Püschel (2025)*. In cases of grid cells overlapping multiple regions, their contribution was split proportionally according to the fractional land area of each region. Uncertainty estimates for regional emissions follow the methodology of *Henne et al. (2016)*, applying a mask vector to the error covariance matrix A to include correlations between grid cells. Gaussian error propagation was used to properly quantify uncertainties for regions composed of multiple grid cells (Püschel, 2025).

4. Results and Interpretation

4.1. Global and Spatial Performance of the Inversion

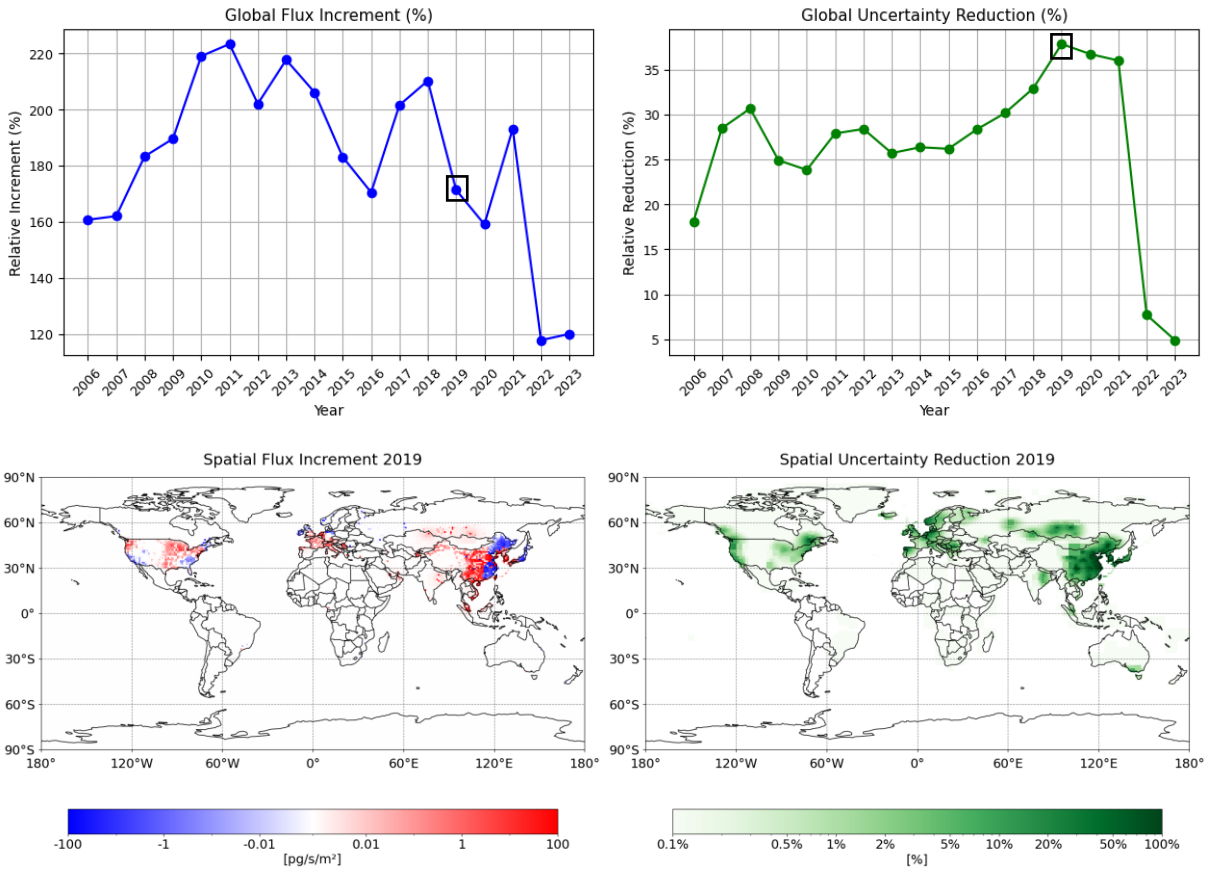

Figure 9: (Top left) Global flux increment from 2006 to 2023 in %, showing overall 120%–220% relative increment above prior estimates. (Top right) Global mean uncertainty reduction over the same period reaching from 5% to almost 40%. (Bottom left) 2019 Flux increment heatmap (in pg/s/m²) ranges from –100 (blue) to 100 (red), highlighting regional emission adjustments resulting from the inversion. (Bottom right) 2019 Uncertainty Reduction Heatmap shows percentage reductions from 0% (white) to 100% (green), illustrating clear spatial variations in uncertainty reduction.

The global performance of FLEXINVERT+ over the period from 2006 to 2023 can be divided into several distinct phases based on the availability of observations (see Figure 3) significantly influencing inversion results. Figure 9 (top left) shows the global flux increment from 2006 – 2023 and (bottom left) its spatial distribution in 2019. As the locations of emitting industries and facilities are generally well-covered by the prior, posterior distribution does not vary much from the prior distribution. A detailed analysis on emission distributions in high emitting areas follows in section 4.3. Prior emission magnitudes on the other hand are highly uncertain and differ significantly from our model posterior results.

In the early years of 2006 - 2010 the inversion showed substantial increases in global flux estimates of 60% - 120% relative to prior values. Correspondingly, the inversion reduced the global mean uncertainty,

pictured in Figure 9 (top right), by approximately 20%–30% compared to the prior error. Peaking in 2008 this local maximum aligns with a local maximum in the number of observations in this year (see Figure 3), reflecting the strong impact of the observational constraint on corrections of emission magnitudes, even in years of limited observations.

In 2011, the total number of observations increased sharply compared to 2010 driven by the introduction of the Shangdianzi (SDZ) continuous measurement site in China and continuous observations from Jungfraujoch (JFJ) in Switzerland (see section 3.2.). Although several new flask measurement sites throughout China and the U.S. were introduced between 2011 and 2015, the total number of observations increased only slightly. However, despite the rise in observational constraint, the relative uncertainty reduction during this phase stayed around 25% - 30% with posterior fluxes typically 70% to 120% higher than priors.

From 2016 the inversion further reduces uncertainty, corresponding to a continuous increase of total observations and observation sites with 2019 marking the peak in both, number of observations and global mean uncertainty reduction of nearly 40%. The increased data availability allowed FLEXINVERT+ to constrain emissions more confidently, reducing uncertainties effectively even as flux adjustments became smaller relative to prior estimates. The 2019 flux increment heatmap (Figure 9 (bottom left)) and the 2019 uncertainty reduction heatmap (Figure 9 (bottom right)) illustrate clear regional differences introduced by the inversion. Posterior emissions show significant adjustments over regions with strong observational constraints like East Asia, Europe and North America highlighting the influence of observations not only on the global total but especially on regional source estimates detailed in section 4.3. Regions with little or no observational coverage remain close to prior estimates, consistent with the inversion's reliance on observational constraint. This finding is supported by substantial reductions in uncertainty over well-observed regions shown in the uncertainty reduction heatmap of Figue 9 (bottom left).

While, 2019 - 2021 marks the phase with the highest observational density and data quality reflected in the uncertainty reductions close to 37% and flux increment of up to 90%, the period 2022–2023 shows a notable decline in inversion performance. Coinciding with a reduction in measurement data availability for these two years, relative flux increments dropped to around 20%–25% and notably uncertainty reduction fell below 10%. Therefore, we do not include these two years in our analysis mainly focusing on the period between 2007 and 2021.

Overall, FLEXINVERT+ shows consistent and substantial adjustments over prior emission estimates throughout most of the 2007–2021 period, with relative flux increases often exceeding 70% and uncertainty reductions reaching up to 40%. However, regional performance varies significantly and is highly dependent on observational coverage. In regions and years with limited observational data, the inversion

relies more heavily on prior constraints highlighting the importance of both, observational coverage and accurate bottom-up a priori data.

4.2. Global Emission Estimates and Political-Economic Context

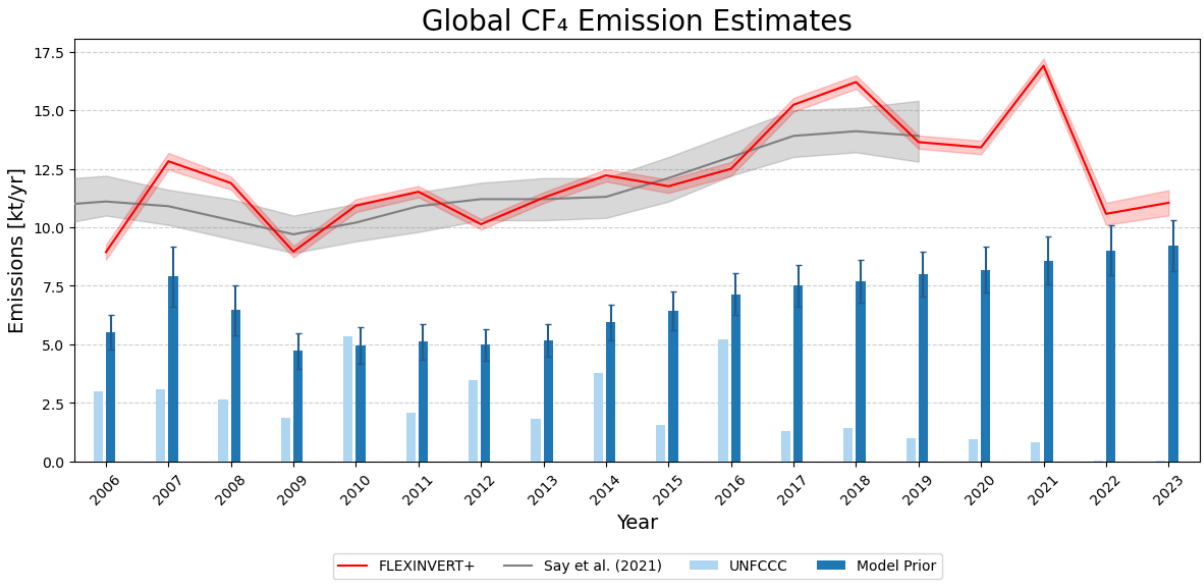

Figure 10: Annual global CF_4 emissions in kt/year from 2006 to 2023 based on top-down (lines) and bottom-up (bars) estimates. FLEXINVERT+ results (red line) and AGAGE 12-box model estimates from Say et al. (2021) (light grey line) are shown with their respective uncertainty bands. Bottom-up inventories include reported emissions from the UNFCCC (United Nations Framework Convention on Climate Change (UNFCCC), 2024) (light blue bars) and the adapted model prior, primarily based on EDGAR (European Commission & Joint Research Centre (JRC), 2023) data (mid-blue bars). Prior uncertainties are indicated by error bars, assuming 100% uncertainty of the emission magnitude per grid cell.

Analyzing our posterior estimates given in Figure 10 shows that modeled values consistently exceed prior values, in some years by a factor of 1.5 to 2, highlighting the effectiveness of atmospheric observation constraints in correcting systematic underestimations in the prior assumptions. This persistent discrepancy reflects the limitations of bottom-up industry-activity-based inventories. When compared to UNFCCC-reported bottom-up values, this gap is even more substantial and persistent throughout the whole studied period with unrealistically high temporal variability in the UNFCCC reported totals. For instance, in 2018 the posterior estimate was over ten times higher than UNFCCC-reported emissions. These large discrepancies in the global total likely stem from incomplete data, since reports are not always annually and not all countries have to report their emissions. However, looking at national emissions reported to the UNFCCC, these gaps often persist underscoring the limitations in current country reporting and revealing persistent underreporting possibly due to highly uncertain, inconsistent and incomplete bottom-up reporting practices and limited monitoring. Given the UNFCCC's central role in

guiding global and national climate policies as described in section 1.3., these findings highlight a critical need of the UNFCCC to verify the accuracy of national reports in order to remain an effective driver of emission control and to support emission reduction efforts at global and national levels. Additionally, our results once more emphasize the findings of many previous top-down studies in that a coherent and dense observation network is crucial for reducing uncertainties of bottom-up emission estimates.

The global posterior results show a clear upward trend with CF_4 emissions increasing by approximately $32\% \pm 3\%$ from 12.8 ± 0.4 kt yr^{-1} in 2007 to 16.9 ± 0.3 kt yr^{-1} in 2021. In general, our posterior emissions match the results of *Say et al. (2021)* with a slight temporal variability. These fluctuations may partly reflect uncertainties inherent in the inversion, but on the other hand some variability might also be linked to economic developments, successful abatement measures or other events influencing emissions.

Figure 11 shows the contributions of the top-ten CF_4 emitting countries or regions to annual global totals. Given that observations in East Asia only start by the end of 2006, the global totals and contributions of 2006 are highly uncertain likely underestimating contributions of China and on the other hand overestimating contributions of other countries. In contrast, more robust inversion results starting in 2007 reveal a great jump in total global emissions as well as in Chinese contributions making up 48%, while the EU contributes 17%, Tajikistan 9% and Russia 7%. The marked drop in emissions in 2009, present in our inversion results as well as in the data of *Say t. al. (2021),* coincides with the aftermath of the 2008 global financial crisis. This event led to reduced industrial output worldwide, including a contraction in aluminum production due to falling demand and prices (Georgitzikis et al., 2021).

The gradually increasing emission levels from 2009 to 2016, rising by $39\% \pm 4\%$, along with slight temporal variability in our posterior results within the uncertainty range of *Say et al. (2021)* suggest a period of global industrial stabilization. Between 2010 and 2016, China and Russia maintained largely constant average contributions of 56% and 11%, respectively. India, Canada, the U.S., Japan and Malaysia contributed less than 6%, while emissions from Tajikistan declined below 1%. EU emissions fell from 11% in 2011 to 5% in 2016 likely linked to increasing abatement efforts as well as to a 7% decline in EU primary and secondary aluminum production since the 2009 crisis and rising energy costs in this period (European Aluminium Association, 2018; European Commission, 2019a).

The rise in emissions from 2016 until 2018 corresponds with economic growth in Asia, particularly in China with a rapid increase in primary aluminum production (International Monetary Fund, 2019), while the EU and Russia exhibit declining trends. At the same time, India with the world's fifth largest bauxite reservoirs intensified aluminum production through infrastructure and energy reforms which may explain the emission contribution of almost 18% in 2018 that was estimated by our inversion (Government of India, 2014; Verma et al., 2015). However, in the case of India, results must be interpreted with caution since observational constraint is low and the model does not perform so well, explained in detail in the following section 4.3.2.

The decline in 2019 and 2020 reflects overlapping developments: In 2019, global primary aluminum production dropped by ~1% (International Aluminium Institute, 2020), partly due to weaker global demand and trade tensions, particularly between the U.S. and China, which dampened industrial activity (Georgitzikis et al., 2021; International Monetary Fund, 2019). Around 80% of the 2018/2019 emission reduction stemmed from China, likely influenced by both slower growth, and ongoing technological transitions. Since 2013, the Chinese government has implemented supply-side reforms to curb excess capacity and reduce environmental impacts by introducing capacity swaps and closing outdated smelters. By 2019, 95% of global production operated under the *Point-Feeder Prebake (PFPB)* technology recommended by the *International Aluminium Institute (IAI)* as this technology reduces anode effects and associated CF_4 emissions (International Aluminium Institute, 2020).

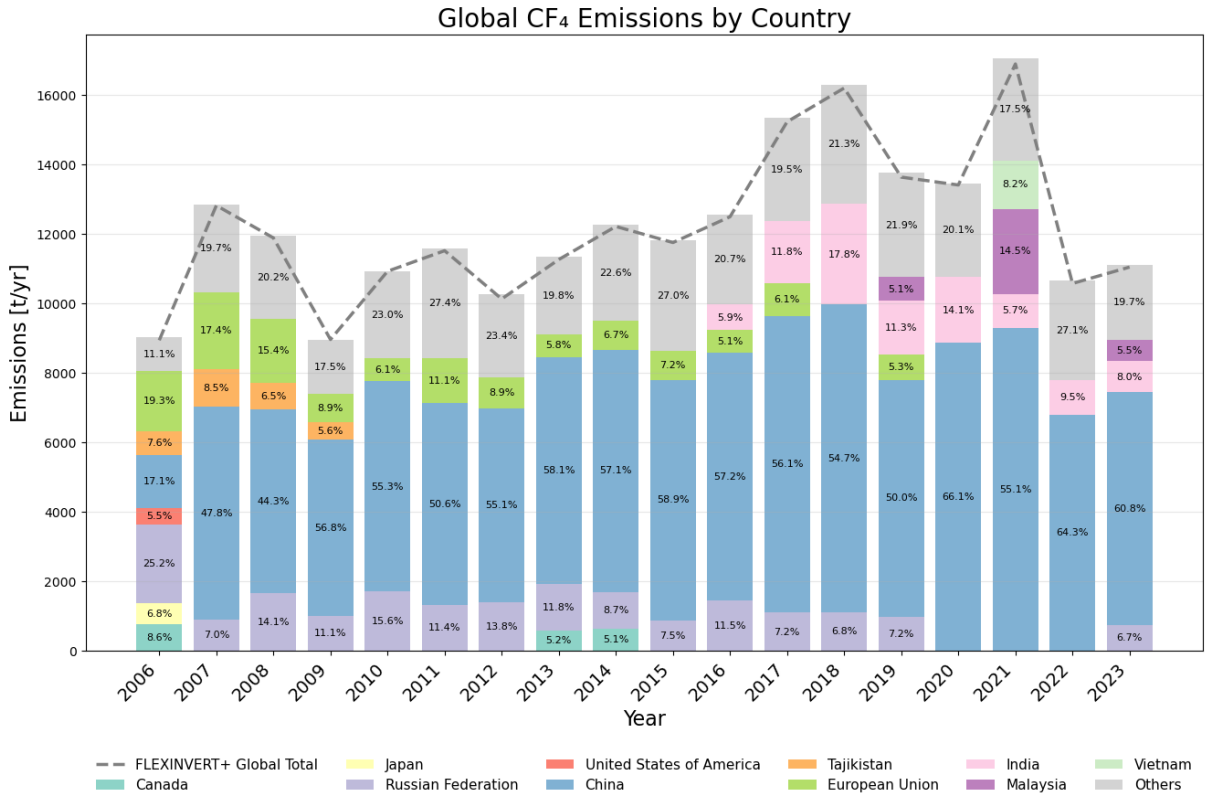

Figure 11: Annual global CF_4 emissions in t/year from 2006 to 2023, with stacked bars showing the percentual contributions of the top 10 emitting countries that contribute at least 5% to the global total (dashed grey line). China (blue) stands out as the major contributor throughout the entire period.

The 2020 emissions are greatly influenced by the global impact of the COVID-19 pandemic, which caused widespread disruption in supply chains and reduced industrial activity. This has likely influenced shifts in global county contributions due to country-specific restrictions and recovery of economies marked by increased contribution by China (57%) and India (14%). Looking at the aluminum industry, the COVID-19 pandemic dampened demand for aluminum mostly in the automotive and construction

sectors. An analysis of the *CM Group (2020)* on behalf of the IAI projected a strong recovery for China in 2021 leading the global post-COVID recovery in aluminum production due to its overcapacity, while in contrast, recovery and demand in Europe and North America was projected to not even be attained within 2022 (Georgitzikis et al., 2021).

This predicted post-COVID increase in 2021 is indeed visible in global emission trends and appears to be driven primarily by China (55%), Malaysia (14%), and Vietnam (8%) (see Figure 11). As explained previously, China's rise is most likely tied to its leading role and overcapacity in primary aluminum production, whereas Malaysia's notable 14% share marks its emergence as a significant contributor. Since 2020, Malaysia's exports rebounded faster than those of other Southeast Asian countries driven by a rising demand for electronics and semiconductors particularly from China and the U.S.. Thus, unlike China, where emissions are predominantly linked to primary aluminum production, Malaysia's increase most likely mainly stems from semiconductor and electronics manufacturing reflecting a regional and sectoral shift in global emission contributions in 2021 (OECD, 2021). Similar to Malaysia, Vietnam's contribution to global CF_4 emissions, peaking in 2021, is closely tied to its rapid industrialization and expanding role in post-COVID restructured global supply chains. In 2021 both, Malaysia and Vietnam, attracted significant foreign direct investment, particularly in electronics and information and communication technology (ICT) manufacturing with CF_4 emitting industries such as semiconductor and display fabrication (OECD, 2021).

As discussed previously, results of 2022 and 2023 must be interpreted with caution as a lack of measurements for these years resulted in minimal uncertainty reductions and close-to-prior values.

These findings demonstrate that global trends in CF_4 emissions are intricately linked to major global events as well as to regional political and economic developments. This underscores the importance of regionally resolved emission patterns for understanding how emissions evolve in response to policy and economic shifts which is crucial for introducing effective reduction strategies.

4.3. National Emission Estimates and Regional Distribution

In this section, we take a closer look at national emission estimates of our inversion and country-level contributions to the global share, focusing on dominant contributors and spatial features in our inversion results. The geographic distribution of CF_4 emissions in the studied period reveals a shift toward emerging economies in South and East Asia with China as the dominant and still rising source of emissions throughout the whole period and India, Malaysia and Vietnam as upcoming emitters since the late 2010s and early 2020s, while contributions of Russia, Japan, the EU and North America are slightly declining.

4.3.1. China

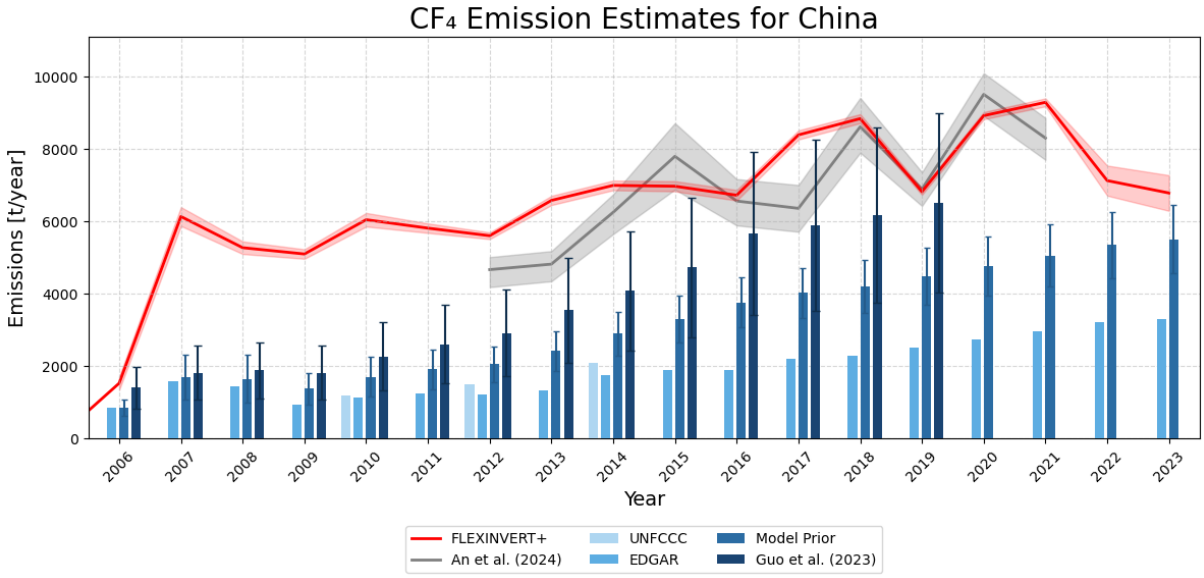

Figure 12: Annual CF_4 emissions in t/year estimated for China from 2006 to 2023 based on top-down (lines) and bottom-up (bars) estimates. FLEXINVERT+ results (red line) are shown alongside top-down estimates by An et al. (2024) (light grey line), both with their respective uncertainty bands. Bottom-up inventories include reported emissions from the UNFCCC (United Nations Framework Convention on Climate Change (UNFCCC), 2024) (light blue bars), our adapted model prior based on EDGAR data (mid-blue bars) and the original EDGAR prior (European Commission & Joint Research Centre (JRC), 2023)) (turquoise bars) as well as bottom-up estimates of Guo et al. (2023) (dark blue bars). Prior uncertainties are indicated by error bars, assuming 100% uncertainty of the emission magnitude per grid cell for our model prior.

Our inversion results for China (see Figure 12) reveal an overall substantial rise in posterior CF_4 emission estimates with an increase of around 52% ± 2.3% from 6.1 ± 0.3 kt yr^{-1} in 2007 to a peak of 9.3 ± 0.1 kt yr^{-1} in 2021. The posterior emissions generally comprise temporal variability with phases of increase and decrease in emissions. In contrast, our adapted prior estimates increase more gradually from 1.7 ± 0.6 kt yr^{-1} to 5.0 ± 0.9 kt yr^{-1} over the same period and tend to reduce prior-posterior discrepancies over time. Yet, the model priors consistently underestimate posterior emissions with discrepancies reaching up to three orders of magnitude in early years. While UNFCCC bottom-up estimates are available only for a few years and underestimate posterior emissions even more, the recent bottom-up estimates by *Guo et al.(2023)*, despite their wide uncertainty range, begin to align with the uncertainty range of our inversion results from 2015 onward and with the uncertainty range of top-down reference values reported by *An et al.(2024)* from 2012 onward. However, all bottom-up estimates fail to capture the observed temporal variability predicted in our results as well as by top-down estimates of *An et al.(2024)*.

A particularly steep increase of 12% ± 3% in posterior emissions is observed between 2016 and 2018 with a drop to 6.8 ± 0.1 kt yr^{-1} in 2019 followed by a strong rebound in 2020 and another peak in 2021. Given that China's emissions make up more than half of the global emissions in most years, Chinese developments significantly drive global trends as seen and explained in detail in section 4.2. The top-down estimates from *An et al.(2024)*, which use the same Chinese atmospheric observations as we do in our study, and our posterior values show strong agreement within predicted uncertainty margins, especially between 2014 and 2021. Although both use the same regional measurements, the alignment proves that our global inversion framework can reproduce regional studies in well-constrained areas. The decline in posterior emissions in 2022 and 2023, likely does not reflect real emission reductions, but rather corresponds to a lack of available East Asian atmospheric measurements resulting in closer-to-prior posterior values. This again may drive the same trend observed in global estimates.

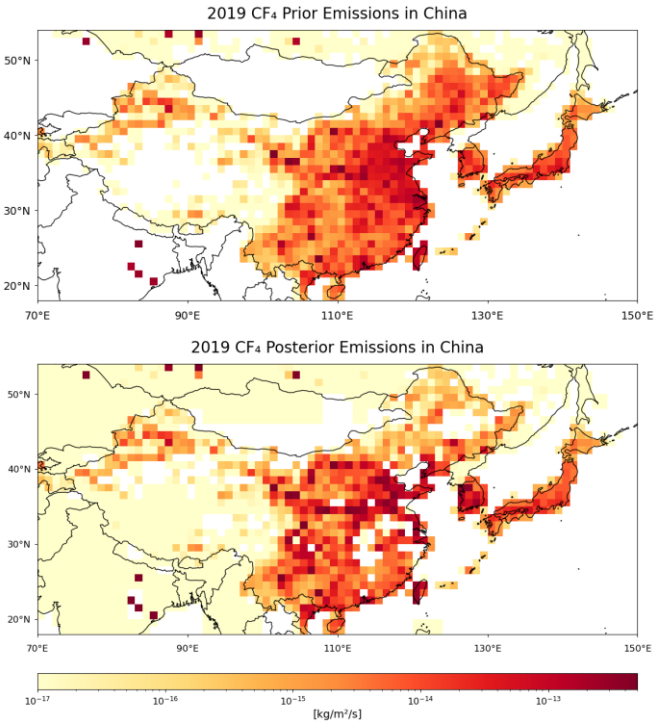

Figure 13: Heatmap of prior (top) and posterior (bottom) emission estimates for China in 2019, with values ranging from 1×10^{-17} (light yellow) to 1×10^{-12} (dark red) kg/m²/s. The maps illustrate the spatial distribution of emissions and reveals the adjustments made by the inversion through the inclusion of observational data.

Comparing the spatial distribution of prior and posterior CF_4 emissions reveals small adjustments made by the inversion. The prior emissions exhibit a more uniform density across industrial regions of eastern China likely reflecting bottom-up estimates based on production activity. In the East of China emissions are adjusted downward (see Figure 13), likely reflecting an overestimated spatial coverage of emissions, while elsewhere posterior estimates get more localized pointing to strong point sources. Constrained by atmospheric measurements, especially covering the East of China through continuous measurements at Gosan observation site, our posterior emissions provide refined spatial features alongside with a high degree of uncertainty reduction. This suggests that while bottom-up inventories often capture emission patterns only broadly based on sectoral activity, the inversion can resolve posterior estimates to point sources in well-constrained areas. In less observed regions however, our results rather highlight the performance of our inversion in correcting for emission magnitude than improving spatial distribution.

4.3.2. India

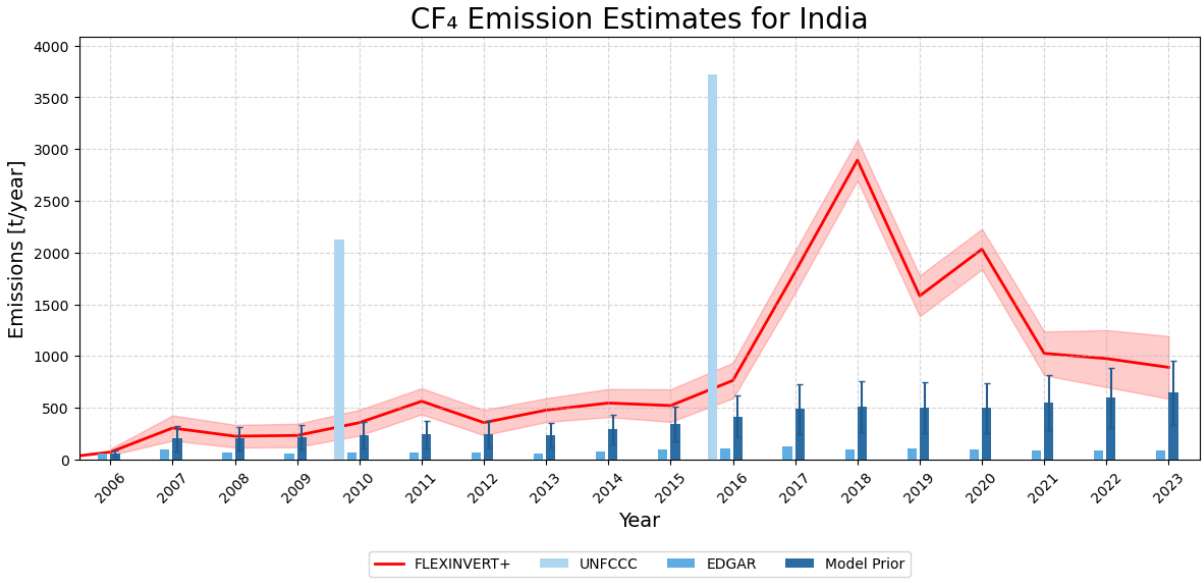

Figure 14: Annual CF_4 emissions in t/year estimated for India from 2006 to 2023 based on top-down (lines) and bottom-up (bars) estimates. FLEXINVERT+ results (red line) are shown with their respective uncertainty bands. Bottom-up inventories include reported emissions from the UNFCCC (United Nations Framework Convention on Climate Change (UNFCCC), 2024) (light blue bars), our adapted model prior based on EDGAR data (mid-blue bars) and the original EDGAR prior (European Commission & Joint Research Centre (JRC), 2023)) (turquoise bars). Prior uncertainties of our model prior are indicated by error bars, assuming 100% uncertainty of the emission magnitude per grid cell.

India as a region with no local atmospheric observations and no nearby ground-based measurement sites is limited in direct observational constraint of CF_4 emissions, leading to results with high uncertainties. Consequently, the same limitations apply to the resulting interpretations. Considering these limitations in combination with our inversion results, India is an interesting case that warrants closer examination. Inversion results of India given in Figure 14 show a sharp increase from 2015 on peaking at 2018. While this trend aligns with a slight increase in observational coverage and the addition of new flask measurement sites in China, which likely contribute to a greater deviation from prior emissions, it is also worth noting that a 58% rise in aluminum production between 2015 and 2018 may have played a role in driving this trend (National Institution for Transforming India (NITI

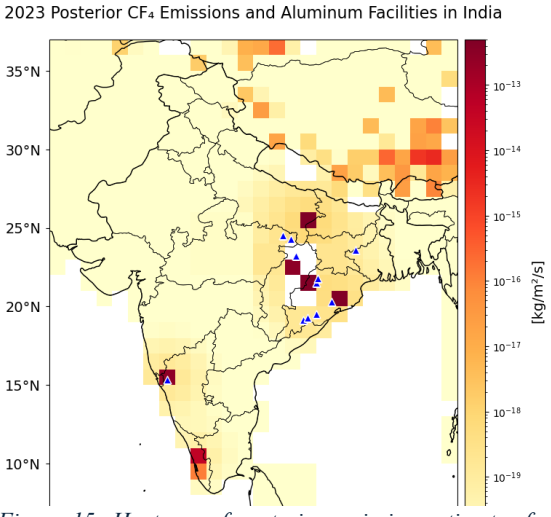

Figure 15: Heatmap of posterior emission estimates for India in 2023, with values ranging from 1×10^{-20} (light yellow) to 1×10^{-12} (dark red) kg/m²/s. The spatial distribution largely resembles the prior estimates due to limited observational constraints. Locations of aluminum facilities reported by the National Institution for Transforming India (National Institution for Transforming India (NITI Aayog), 2025) (blue triangles) correspond well with the emission pattern, suggesting that both prior and posterior emissions are primarily informed by data from the aluminum industry.

Aayog), 2025). Given the reported aluminum production, it is striking that for India prior values of EDGAR are unrealistically low, while the unregular UNFCCC reports are likely overestimated. Our adapted prior aligns closely with our posterior in early years of the inversion, when India was less constrained with measurements from China, but seems to underestimate emissions in the late 2010s and early 2020s when compared to posterior estimates that differ by factors of up to 5. However, posterior values might also be overestimated. Generally, and specifically in the case of India, uncertainties are likely underestimated, which is also why spatial distribution is strongly influenced by prior assumptions. It is likely that prior estimates mainly include emissions of the aluminum industry, since its point-source pattern mostly matches the locations of aluminum facilities reported by *India's National Institution for Transforming (NITI Aayog)* (see Figure 15) (National Institution for Transforming India (NITI Aayog), 2025). Ignoring the fact that it remains unclear whether all of the listed facilities were operating in 2023, there are some aluminum facilities with no significant assigned emissions as well as estimated emission hot-spots far away from known aluminum facilities questioning the accuracy of the prior and suggesting that there might be other unconsidered emitting sectors.

Despite the high uncertainty in Indian posterior emission estimates, reports like *the Minerals Yearbook of the U.S. Geological Survey* (Renaud, 2023) indicating that India became the third-largest aluminum producer in 2017 and rose to second-largest in 2018 align with the trend in our Indian emission estimates. This suggests that the inversion likely captured Indian emissions within global signals from distant observations and attributed them back to India through transport modeling.

4.3.3. Malaysia, Singapore and Vietnam

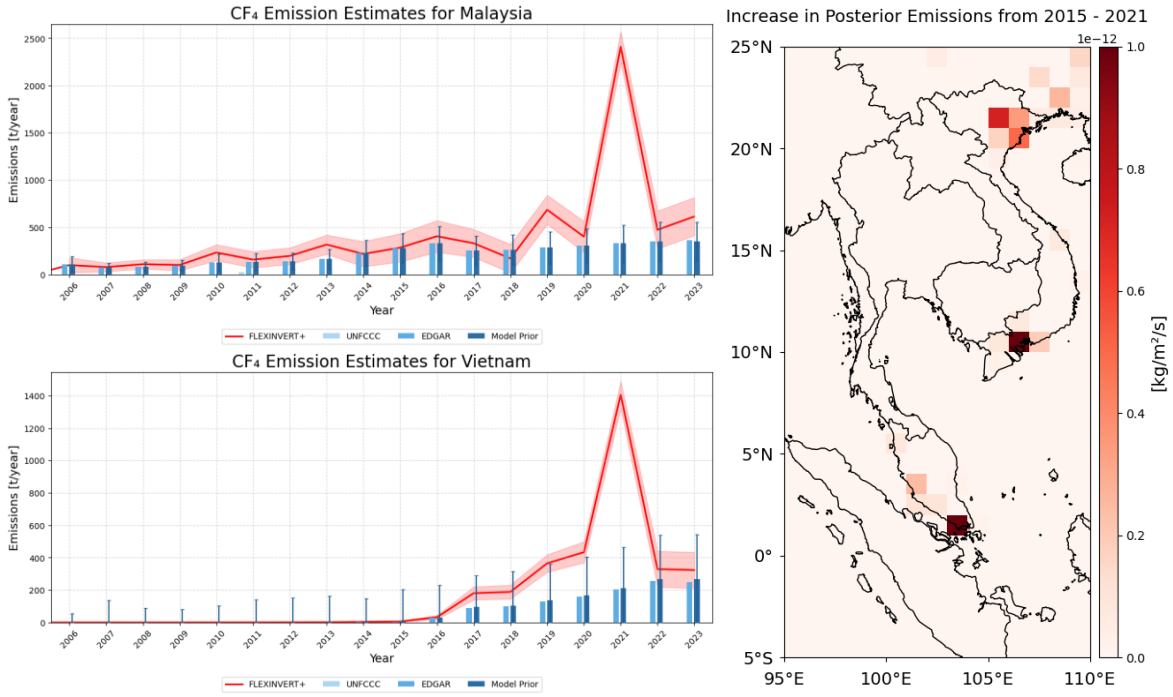

Figure 16: Annual CF_4 emissions in t/year estimated for Malaysia (top left) and Vietnam (bottom left) from 2006 to 2023 based on top-down (lines) and bottom-up (bars) estimates. FLEXINVERT+ results (red line) are shown with their respective uncertainty bands. Bottom-up inventories include reported emissions from the UNFCCC (United Nations Framework Convention on Climate Change (UNFCCC), 2024) (light blue bars) and the model prior, based on EDGAR (European Commission & Joint Research Centre (JRC), 2023) data (mid-blue bars). Prior uncertainties are indicated by error bars, assuming 100% uncertainty of the emission magnitude per grid cell. (Right) Heatmap of posterior emission increase from 2015 to 2021 in Malaysia, Singapore, and Vietnam, with values ranging from 0 (light red) to 1×10^{-12} (dark red) kg/m²/s. The map highlights three major emission hotspots driving this increase, located in Hanoi, Ho Chi Minh City, and the Johor Bahru/Singapore region.

Similar to India, Malaysia, Singapore, and Vietnam are poorly constrained by observations, with coverage limited to distant Chinese observation sites that primarily cover northern Vietnam. As a result, inversion outputs for these regions given in Figure 16 (top and bottom left) should be interpreted with caution, and the associated uncertainties are likely underestimated. As in the case of India, the growing discrepancy between prior and posterior estimates coincides with the addition of new flask measurement sites in China, which may be revealing previously undetected mismatches. The sharp spikes in 2021 posterior emissions of 2.4 ± 0.2 kt/yr^{-1} for Malaysia and 1.4 ± 0.1 kt/yr^{-1} for Vietnam are likely overestimated and may reflect the influence of episodic high-emission events in China. Nevertheless, our transport model attributes some signal to the South East Asian region, and a general emission increase from 2015 to 2021 aligns with regional economic trends like a 49% rise in Vietnam's GDP and a 24% rise in Malaysia's during this period, likely driven by post-COVID industrial recovery as discussed in section 4.2. (World Bank, 2023). Spatial distribution of posterior emission estimates, while likely carrying high uncertainties, show country-wide emissions for both countries in 2021. The posterior emission increase from 2015 – 2021 visualized in Figure 16 (right), however, pin-points a few major hot-

spots around Hanoi, Ho-Chi-Minh City and Johor Bahru/Singapore that are likely responsible for the drastic emission increase.

As seen in other emerging economies like India, prior emission inventories often fail to adequately reflect such rapid changes, likely underestimating growth in industrial emissions from fast-developing sectors. Posterior estimates can offer a more responsive tracking of newly evolving emission patterns. However, this trend detection is often uncertain and should be seen as a preliminary indication, especially given the limited observational coverage in many of these emerging regions. Nevertheless, these findings show the potential of a global inversion in early detection of emerging trends, even with limited, far away observation constraint potentially suggesting new emission sources that may be worth further investigations. This further highlights the importance of up-to-date and responsive top-down emission estimation. As for other countries, the last two years suffer from the lack of observations and, thus, the posterior emissions remain close to the prior ones.

4.3.4. Europe and the EU

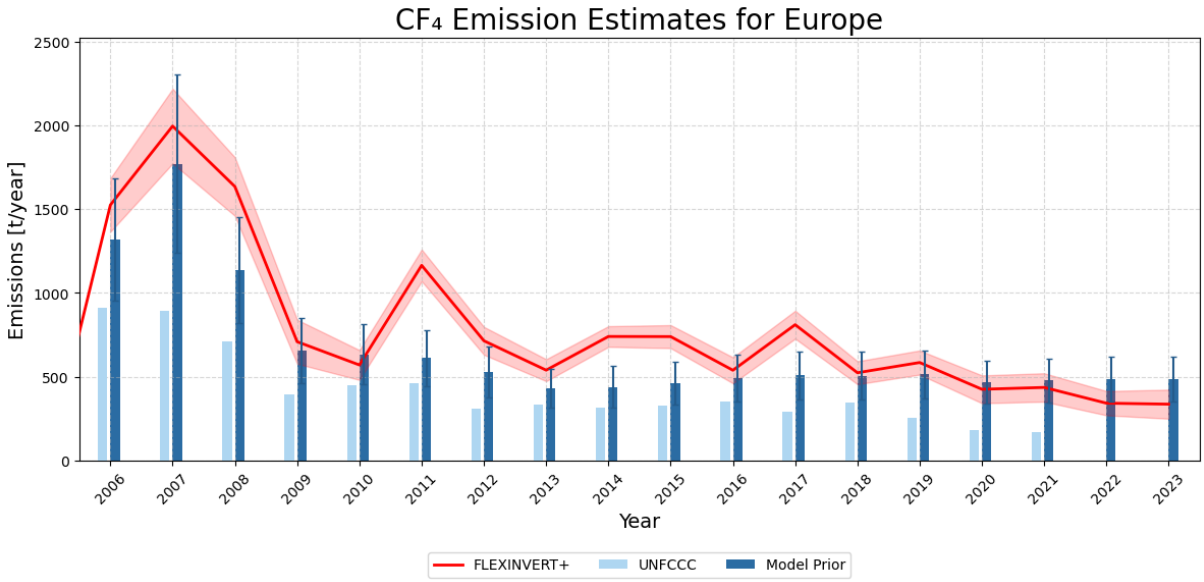

Figure 17: Annual CF_4 emissions in t/year estimated for Europe from 2006 to 2023 based on top-down (lines) and bottom-up (bars) estimates. FLEXINVERT+ results (red line) are shown with their respective uncertainty bands. Bottom-up inventories include reported emissions from the UNFCCC (United Nations Framework Convention on Climate Change (UNFCCC), 2024) (light blue bars) and the model prior, based on EDGAR (European Commission & Joint Research Centre (JRC), 2023) data (mid-blue bars). Prior uncertainties are indicated by error bars, assuming 100% uncertainty of the emission magnitude per grid cell.

Unlike other regions, posterior emissions in Europe given in Figure 17 generally fall within the uncertainty range of the prior estimates, with some exceptions. However, a noticeable shift occurs in the prior-posterior discrepancy. Earlier years show lower prior values compared to the posterior indicating that

the inversion identifies an underestimation in the priors. From 2020 onward, this pattern reverses, suggesting an overestimation in prior emissions. The final two years, however, are significantly less constrained by observational data, resulting in greater uncertainty in the posterior estimates. As in most other regions, UNFCCC inventories likely underestimate emissions by up to a factor of two, probably due to incomplete national reporting or underestimated emission factors.

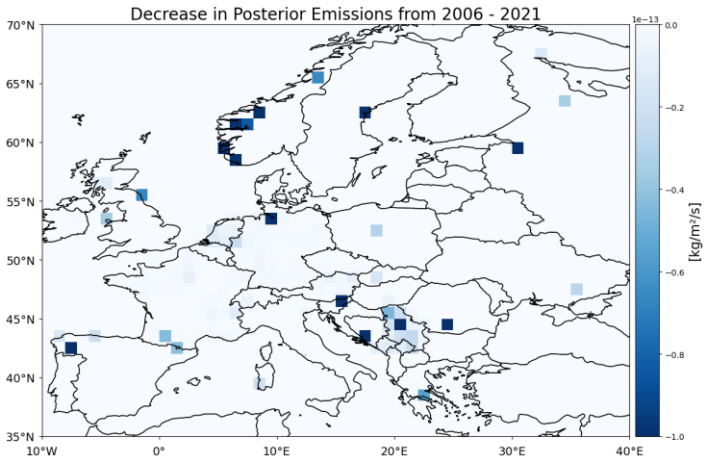

Figure 18: Heatmap of posterior emission decrease from 2006 to 2021 in Europe, with values ranging from 0 (light blue) to -1×10⁻¹³ (dark blue) kg/m²/s. The map reveals multiple hotspots of emission reduction, likely corresponding to individual facilities.

In total, European emissions show a drastic decline of 78% ± 18% from 2007 pre-crisis levels to 2021. The 2009 financial crisis, which caused a first drop in European emissions was followed by an overall long-term downward trend (see section 4.2.), that likely reflects broader political, economic, and technological transformations across Europe. This substantial reduction in European emissions occurred without a corresponding decline in primary aluminum production. From 2006 to 2023 Western and Central European aluminum production fell only by 35% compared to an emission decline of 78% ± 22%. Production rates mainly dropped between 2008 and 2014 and became relatively stable since then (International Aluminium Institute, 2024). Despite this stabilization in this high emitting industry, emissions continued to decline, suggesting that emission reductions were also driven by effective abatement measures. According to *The European Aluminium Environmental Profile Report (2018)*, the European aluminum sector has increasingly adopted best available technologies driven by EU projects like the *AGRAL (Advanced Green Aluminium anode) project* from 2015 – 2018 (European Aluminium Association, 2018; European Commission Joint Research Centre, 2015). Potentially, further EU environmental regulations like the *EU Emissions Trading System* and the *European Green Deal* as well competitive pressure have further driven this trend.

Declining emissions in Europe are a general broad trend among Europe's major aluminum-producing countries. Figure 18 visualizes the decrease of posterior emissions from 2006 to 2021 and reveals point-sources driving the European decline in CF_4 emissions which likely resembles facilities that significantly reduced their emissions either by curbing production or introducing efficient abatement measures. Figure 19 supplements this reduction trend with country contributions to European emissions. While country contributions among the top emitters in recent years exhibit stronger fluctuations, due to economic crisis and more uncertain inversion results in 2022 and 2023, Romania overall recorded the highest

posterior emissions, followed by Croatia and Spain. From 2006 until 2021 emissions in Romania declined by 68%, in Croatia by 63% and in Spain by 85% with Germany (88%), Greece (21%), the Netherlands (56%) and Norway (91%) following this trend. In summary, the European CF_4 emission reductions from 2006 to 2023 offer compelling evidence of successful emission reduction while maintaining substantial levels of primary aluminum production, which is likely driven by political frameworks, voluntary efforts or economic pressure. Europe's case highlights the potential of policy-driven innovation for achieving sustainable transitions.

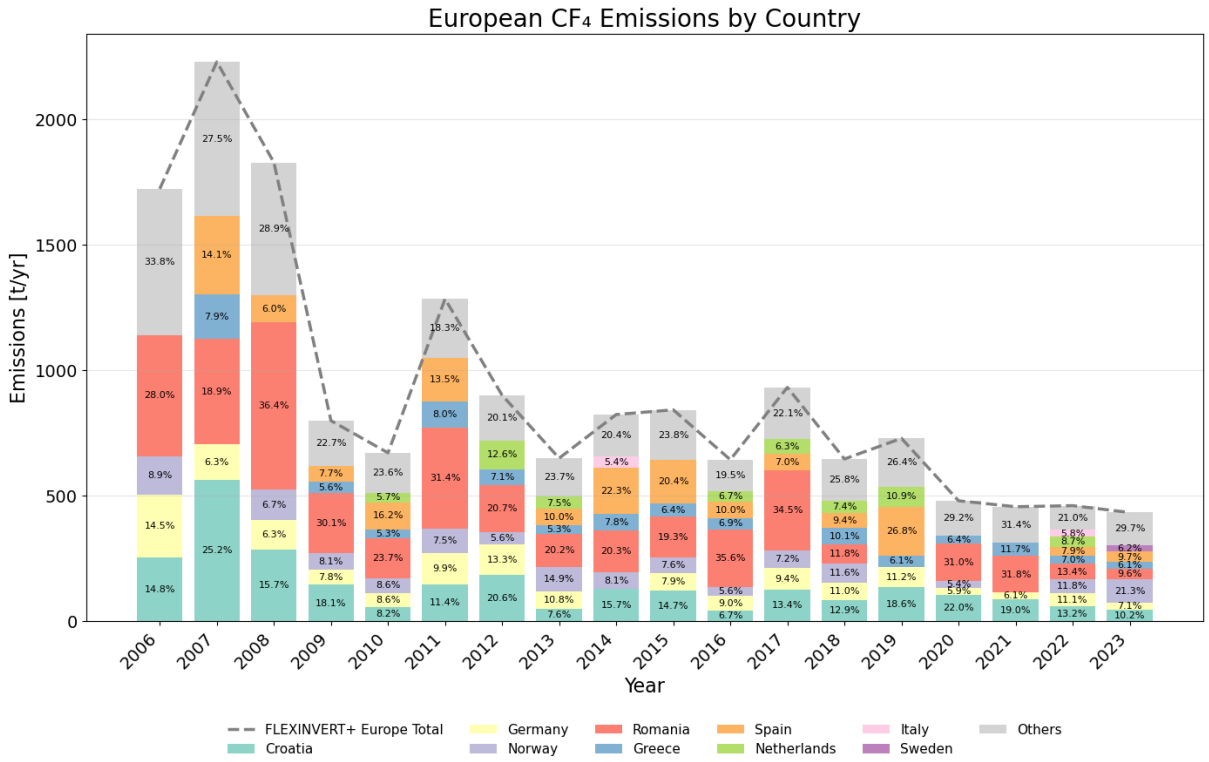

Figure 19: Annual CF_4 emissions estimated for Europe in t/year from 2006 to 2023, with stacked bars showing the percentual contributions of the top 10 emitting countries that contribute at least 5% to the European total (dashed grey line). While contributions from countries generally vary considerably over the study period, Romania (red), Croatia (turquoise), and Spain (orange) exhibit the largest annual contributions in most years.

4.3.5. United States of America

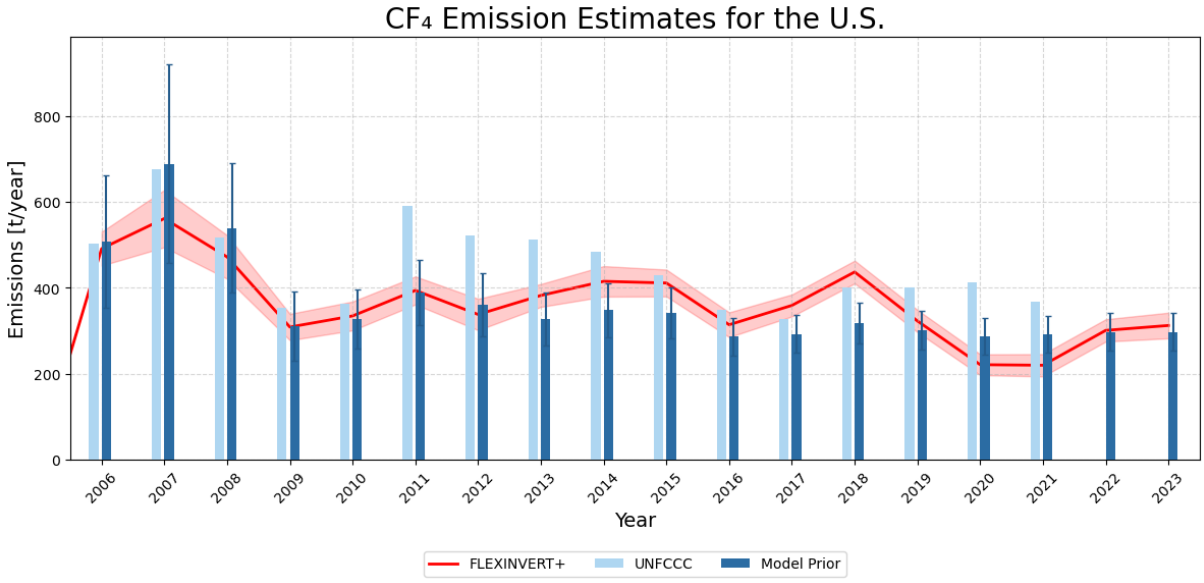

Figure 20: Annual CF_4 emissions in t/year estimated for Europe from 2006 to 2023 based on top-down (lines) and bottom-up (bars) estimates. FLEXINVERT+ results (red line) are shown with their respective uncertainty bands. Bottom-up inventories include reported emissions from the UNFCCC (United Nations Framework Convention on Climate Change (UNFCCC), 2024) (light blue bars) and the model prior, based on EDGAR (European Commission & Joint Research Centre (JRC), 2023) data (mid-blue bars). Prior uncertainties are indicated by error bars, assuming 100% uncertainty of the emission magnitude per grid cell.

CF_4 emissions of the U.S. visualized in Figure 20 are characterized by relatively stable and low CF_4 emissions over the 2006–2023 period with global contributions of 4% in 2007 declining below 3% in 2023. Over the studied period emissions appear largely stable with a dip in 2009 and 2020/2021 during the financial and the COVID-19 crisis respectively. A slight rise between 2015 and 2018 is consistent with economic growth in the U.S. indicated by a GDP growth of more than 7% (World Bank, 2023).

Notably, unlike most other regions posterior estimates of the U.S. closely track the EDGAR and the UNFCCC prior, with minor deviations reflecting the impact of atmospheric constraints. This means that the country's bottom-up prior inventories are well-aligned with top-down estimates of the comparably dense observation network. In most years the variations rarely exceed ±60 t/year. This close agreement suggests an efficient emission reporting framework. This finding is supported by Figure 21 showing the spatial distribution of 2019 posterior CF_4 emissions from our inversion aligning well with the overlaid facility locations of aluminum (blue triangles) and electronics manufacturing (blue circles) facilities that report PFC emissions to the EPA (U.S. Environmental Protection Agency, 2025). In 2016, of the 53 facilities reporting, 52 were semiconductor manufacturers known as CF_4 emitting industry (U.S. Environmental Protection Agency, 2018). Hotspots of posterior emissions are spatially aligned with major aluminum industry in the East and semiconductor clusters in the Southwest and along the East-coast. The integration of facility data from EPA-reported PFC emissions further verifies the attribution of CF_4

to specific industrial sectors, underscoring the importance of incorporating such bottom-up information for interpreting top-down results. Thus, the United States serves as a key example of closely monitored and transparently reported CF_4 emissions, highlighting the role of the U.S. Environmental Protection Agency (EPA) as a centralized authority for monitoring, reporting, and political-economic action through initiatives like the *Greenhouse Gas Reporting Program*, the *VAIP* or the *SNAP program* explained in detail in see section 1.3.

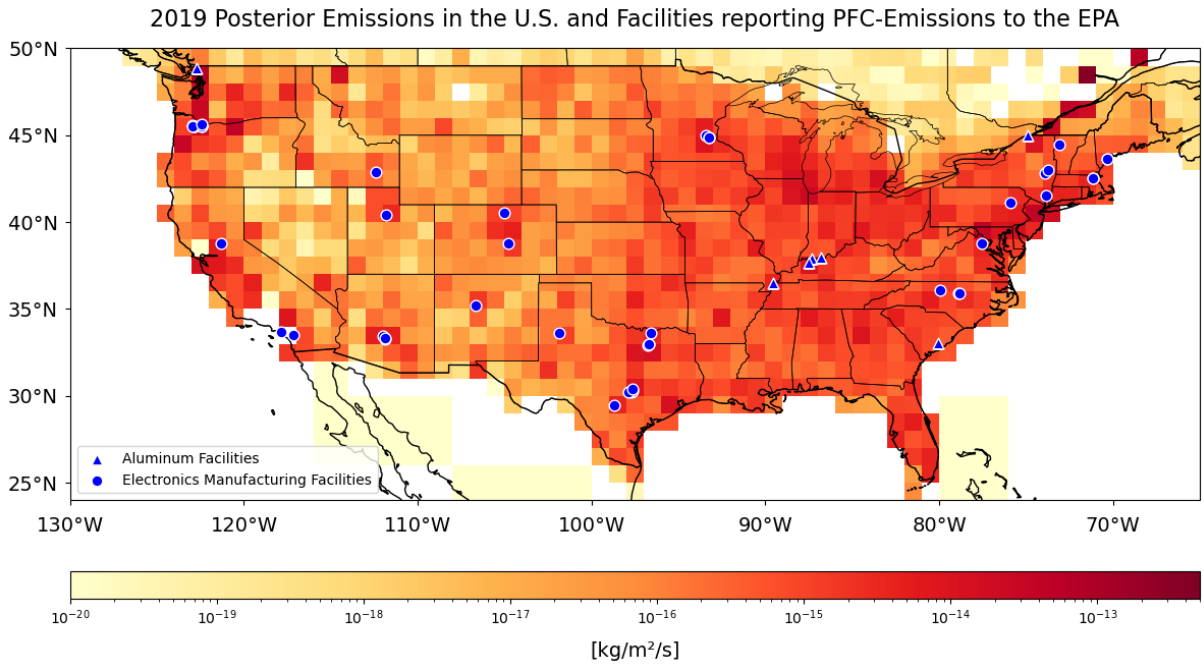

Figure 21: Heatmap of 2019 posterior emission estimates in the U.S., with values ranging from 1×10^{-20} (light yellow) to 1×10^{-12} (dark red) kg/m²/s. The spatial distribution highlights that posterior emissions at least partly associated with aluminum (blue triangles) and electronics manufacturing (blue circles) facilities reporting PFC emissions to the EPA (U.S. Environmental Protection Agency, 2025).

4.4. Top-Down vs. Bottom-Up Discrepancies

As already observed across the national and global results, explained in detail in section 4.2. and 4.3., the analysis of posterior-to-prior emission differences given in Figure 22 offers deeper insight into the extent to which bottom-up reported CF_4 emissions deviate from observation-constrained top-down estimates. Positive discrepancies, where top-down estimates exceed bottom-up values, dominate the global signal throughout the study period, comprising 65–85% of the data, and indicate systematic underestimation in prior inventories. Negative discrepancies remain below 20% and are thus offset by the stronger positive signals, resulting in global top-down values that consistently surpass bottom-up totals. China is the largest contributor to these global discrepancies, accounting for +40% to over +60% of the total. Russia and Tajikistan contribute notably in earlier years, while India and Malaysia emerge in the late 2010's. Among negative contributors, Canada stands out with up to -10%, reflecting an overestimation

of prior emissions, though such cases are rare and relatively small. These patterns highlight the critical role of top-down inversions in detecting potential biases in bottom-up inventories. While uncertainties in the inversion process persist, the magnitude of observed discrepancies strongly supports the integration of measurement-constrained top-down estimates into national and international reporting frameworks. Overall, the findings underscore the value of top-down approaches for improving bottom-up accuracy and informing climate policy.

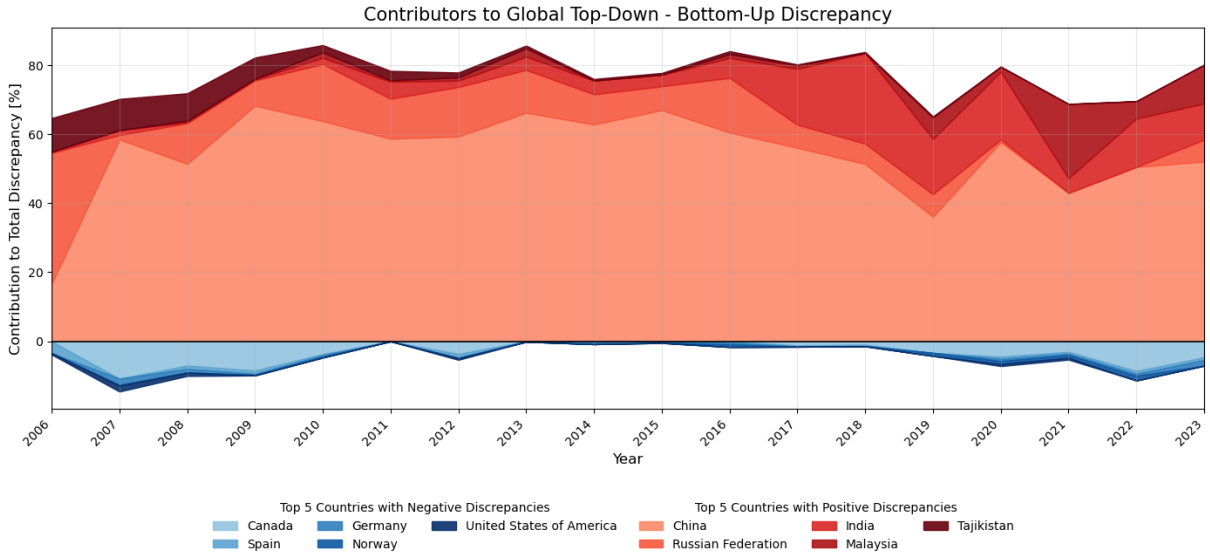

Figure 22: Annual contribution of the top five countries to the global discrepancy between top-down and bottom-up emission estimates from 2006 to 2023. Positive contributions (shades of red) indicate countries where top-down estimates exceed bottom-up inventories, while negative contributions (shades of blue) reflect the opposite. The stacked bars show the percentual share of each country to the total global discrepancy per year, revealing dominating positive discrepancies and China with highest top-down to bottom-up discrepancies.

5. Conclusion

This top-down analysis of regionally resolved global CF_4 emission estimates from 2006 to 2023 obtained by inverse modeling with FLEXINVERT+, based on a Bayesian framework (Thompson & Stohl, 2014), provides insights into global totals, regional emission patterns, bottom-up inventory discrepancies, and the critical role of atmospheric observations in constraining the model.

Although being known as a compound with no atmospheric sinks and an atmospheric lifetime of approximately 50,000 years (Burkholder et al., 2019), CF_4 is often overlooked in both international and national policy frameworks and lacks specific emission restrictions. Our results, by contrast, highlight the importance of accurately reporting and monitoring emissions, which appear to be consistently underestimated in international inventories. The inversion results show consistent and substantial adjustments to prior emissions throughout most of the period. Across the study period, 65% - 85% of national-

level posterior estimates exceed their respective prior values and so do the total global posterior emissions, with relative increases often surpassing 70%. These systematic positive discrepancies suggest that bottom-up inventories tend to significantly underestimate CF_4 emissions, particularly in China, which exhibits the largest top-down to bottom-up discrepancies, accounting for up to 60% of the global total discrepancy. Consequently, our study reveals major limitations in bottom-up reporting with prior datasets often providing highly uncertain, incomplete estimates, lacking spatial resolution or reporting only total PFC values. UNFCCC-reported CF_4 emissions show particularly stark mismatches with our top-down results, reflecting incomplete reporting and uncertainty in bottom-up accounting methods. These mismatches emphasize the need for stronger institutional frameworks and independent verification systems.

Aside from prior accuracy, the inversion's performance, which achieves posterior uncertainty reductions of up to 40%, strongly depends on the availability and quality of atmospheric observations. Regions and years with limited observational data, particularly at the start (2006) and end (2022–2023) of the study period, exhibit reduced inversion performance, reaffirming the role of long-term, spatially distributed monitoring networks.

Our global posterior emission results reveal an overall increase of approximately 32% from 2007 to 2021 with inherent temporal variability reflecting economic and industrial developments, like the financial crisis in 2008/2009, the COVID-19 pandemic in 2020/2021 or economic growth linked to production rates in aluminum, semiconductor or other CF_4 emitting industries. China emerges as the dominant source, contributing more than 50% to global totals throughout most of the years. Expanding observational coverage in East Asia, especially in China, until 2021 improves the model's regional performance and helps to track emission trends even in data-sparse neighboring countries. Based on the limited observational data available for other Asian regions, our inversion suggests Malaysia, Vietnam, and particularly India as growing emission contributors since the late 2010s, though with considerable uncertainty. These findings highlight the potential of a global inversion to detect shifting emission patterns and emerging sources earlier than bottom-up systems might do. In contrast to Asia, Europe and the United States exhibit declining or stable emissions likely driven by successful implementation of abatement technologies and slightly decreasing industry activity (European Aluminium Association, 2018; International Aluminium Institute, 2024). Notably, both cases show comparably good agreement between posterior and prior estimates, which is likely a result of more reliable emissions reporting and monitoring through centralized instances like the EPA for example. Together, these two examples likely demonstrate the effectiveness of well-informed emission reporting in driving the implementation of effective abatement measures.

Overall, the results from FLEXINVERT+ highlight the potential of global inversions not only for quantifying total or single localized CF_4 emissions, but also for providing a comprehensive overview of regionally resolved global estimates that link emission trends to specific regional contributions and developments. This enables the identification of broader patterns like the systematic discrepancies between national bottom-up inventories and top-down estimates. The overall rising global emission trends emphasize the need for more international efforts in both improved monitoring and more accurate emission reporting, particularly in under-regulated emerging emission hot-spots. To achieve this, our results suggest a stronger integration of top-down approaches into national and international reporting frameworks in order to shed more light on the impact of this long-lived and extremely potent greenhouse gas and prevent long-term climatic consequences from ongoing industrial emissions (Burkholder et al., 2019).

Acknowledgements

I would like to express my gratitude to the NOAA team and the AGAGE team for providing valuable measurement data, as well as the team at CMA for carrying out measurements in China. AGAGE is primarily supported by grants from the National Aeronautics and Space Administration (USA) to the Massachusetts Institute of Technology and the Scripps Institution of Oceanography with additional operational support by CSIRO and BoM (Australia), NRF (South Korea), FOEN (Switzerland), DESNZ (Ireland), BMBF (Germany), and NILU (Norway).

Further, I am especially thankful to Michael Blaschek and Benjamin Püschel for their technical support and insightful discussions, to Andreas Stohl and Martin Vojta for their supportive supervision throughout this work, and to Lucie, Lisa, Julia, Raoul, and Luis for their continuous encouragement.

References

An, M., Prinn, R. G., Western, L. M., Yao, B., Zhao, X., Kim, J., Mühle, J., Chi, W., Harth, C. M., Hu, J., Ganesan, A. L., & Rigby, M. (2024). Substantial increase in perfluorocarbons CF(4) (PFC-14) and C(2)F(6) (PFC-116) emissions in China. *Proceedings of the National Academy of Sciences of the United States of America*, *121*(30), e2400168121. https://doi.org/10.1073/pnas.2400168121

Arnold, T., Manning, A. J., Kim, J., Li, S., Webster, H., Thomson, D., Mühle, J., Weiss, R. F., Park, S., & O'Doherty, S. (2018). Inverse modelling of CF4 and NF3 emissions in East Asia. *Atmospheric Chemistry and Physics*, *18*(18), 13305–13320. https://doi.org/10.5194/acp-18-13305-2018

Bakels, L., Tatsii, D., Tipka, A., Thompson, R., Dütsch, M., Blaschek, M., Seibert, P., Baier, K., Bucci, S., Cassiani, M., Eckhardt, S., Groot Zwaaftink, C., Henne, S., Kaufmann, P., Lechner, V., Maurer, C., Mulder, M. D., Pisso, I., Plach, A., … Stohl, A. (2024). FLEXPART version 11: Improved accuracy, efficiency, and flexibility. *Geoscientific Model Development*, *17*(21), 7595–7627. https://doi.org/10.5194/gmd-17-7595-2024

Burkholder, J. B., Hodnebrog, Ø., & Orkin, V. L. (2019). *Annex 1: Summary of abundances, lifetimes, ozone depletion potentials (ODPs), radiative efficiencies (REs), global warming potentials (GWPs), and global temperature change potentials (GTPs)* (Vol. 58). Global Ozone Research and Monitoring Project, World Meteorological Organization. https://csl.noaa.gov/assessments/ozone/2018/downloads/AppendixA_2018OzoneAssessment.pdf

Cai, B., Liu, H., Kou, F., Yang, Y., Yao, B., Chen, X., Wong, D. S., Zhang, L., Li, J., Kuang, G., Chen, L., Zheng, J., Guan, D., & Shan, Y. (2018). Estimating perfluorocarbon emission factors for industrial rare earth metal electrolysis. *Resources, Conservation and Recycling*, *136*, 315–323. https://doi.org/10.1016/j.resconrec.2018.04.018

China's National People's Congress. (2011). *The 12th Five-Year Plan for Economic and Social Development (2011–2015)*. https://policy.asiapacificenergy.org/node/37

Cicerone, R. J. (1979). Atmospheric Carbon Tetrafluoride: A Nearly Inert Gas. *Science*, *206*(4414), 59–61. https://doi.org/10.1126/science.206.4414.59

Clappier, A., Pisoni, E., & Thunis, P. (2015). A new approach to design source–receptor relationships for air quality modelling. *Environmental Modelling & Software*, *74*, 66–74. https://doi.org/10.1016/j.envsoft.2015.09.007

Dunse, B. L., Derek, N., Fraser, P. J., Krummel, P. B., & Steele, L. P. (2020). *Australian and Global HFC, PFC, Sulfur Hexafluoride, Nitrogen Trifluoride and Sulfuryl Fluoride Emissions* (pp. vi, 42). CSIRO Oceans and Atmosphere, Climate Science Centre.

Dutton, G., Elkins, J., Hall, B., & NOAA ESRL. (2017). *Earth System Research Laboratory Halocarbons and Other Atmospheric Trace Gases Chromatograph for Atmospheric Trace Species (CATS) Measurements* (Version Version 1) [Dataset]. https://doi.org/doi:10.7289/V5X0659V [25.01.2024]

European Aluminium Association. (2018). *European Aluminium Environmental Profile Report 2018: Executive Summary*. https://de.slideshare.net/slideshow/european-aluminium-environmental-profile-report-2018-executive-summary/88499791

European Commission. (2019a). *Energy Prices and Costs in Europe: Commission Staff Working Document. Part 6/11* [SWD(2019) 1 final]. European Commission. https://eur-lex.europa.eu/legal-content/EN/TXT/?uri=SWD%3A2019%3A1%3AFIN

European Commission. (2019b). *The European Green Deal*. https://eur-lex.europa.eu/legal-content/EN/TXT/?uri=CELEX:52019DC0640

European Commission Joint Research Centre. (2015). *Development of an optimum AGRAL cermet manufacturing process for aluminium inert anode application*. https://ses.jrc.ec.europa.eu/eirie/en/project/development-optimum-agral-cermet-manufacturing-process-aluminium-inert-anode-application

European Commission, & Joint Research Centre (JRC). (2023). *EDGAR (Emissions Database for Global Atmospheric Research) Community GHG Database, a collaboration between the European Commission, Joint Research Centre (JRC), the International Energy Agency (IEA), and comprising IEA-EDGAR CO2, EDGAR CH4, EDGAR N2O, EDGAR F-GASES* (Version version 8.0) [Dataset]. https://edgar.jrc.ec.europa.eu/dataset_ghg80#sources

European Parliament and Council. (2021). *Regulation (EU) 2021/1119 establishing the framework for achieving climate neutrality (European Climate Law)*. https://eur-lex.europa.eu/legal-content/EN/TXT/?uri=CELEX:32021R1119

European Parliament Council. (2024). *Regulation (EU) 2024/590 of the European Parliament and of the Council of 7 February 2024 on substances that deplete the ozone layer, and repealing Regulation (EC) No 1005/2009*. http://data.europa.eu/eli/reg/2024/590/oj

European Union. (2003). *Directive 2003/87/EC of the European Parliament and of the Council of 13 October 2003 establishing a scheme for greenhouse gas emission allowance trading within the Community and amending Council Directive 96/61/EC*. https://eur-lex.europa.eu/legal-content/EN/TXT/?uri=CELEX%3A32003L0087

European Union. (2014). *Regulation (EU) No 517/2014 of the European Parliament and of the Council of 16 April 2014 on fluorinated greenhouse gases*. https://eur-lex.europa.eu/legal-content/EN/TXT/?uri=CELEX%3A32014R0517

Gandarillas, V., Joshy, A. J., Sperry, M. Z., Ivanov, A. K., & Hwang, J. T. (2024). A graph-based methodology for constructing computational models that automates adjoint-based sensitivity analysis. *Structural and Multidisciplinary Optimization*, *67*(5), 76. https://doi.org/10.1007/s00158-024-03792-0

Georgitzikis, K., Nita, V., Ciupagea, C., & Garbossa, E. (2021). *The aftermath of US tariffs on aluminium imports. An assessment of tariff impacts and a review of the EU aluminium industry*. https://doi.org/10.2760/46784

Government of India. (2014). *Make in India*. https://www.pmindia.gov.in/en/major_initiatives/make-in-india/

Government of the People's Republic of China. (2016). *The 13th Five-Year Plan for Economic and Social Development of the People's Republic of China (2016–2020)*. https://en.ndrc.gov.cn/policies/202105/P020210527785800103339.pdf

Groot Zwaaftink, C. D., Henne, S., Thompson, R. L., Dlugokencky, E. J., Machida, T., Paris, J.-D., Sasakawa, M., Segers, A., Sweeney, C., & Stohl, A. (2018). Three-dimensional methane distribution simulated with FLEXPART 8-CTM-1.1 constrained with observation data. *Geoscientific Model Development*, *11*(11), 4469–4487. https://doi.org/10.5194/gmd-11-4469-2018

Guo, L., & Fang, X. (2024). Revealing the global emission gaps for fully fluorinated greenhouse gases. *Scientific Reports*, *14*(1), 8753. https://doi.org/10.1038/s41598-024-58504-x

Guo, L., Yang, Y., Fraser, P. J., Velders, G. J. M., Liu, Z., Cui, D., Quan, J., Cai, Z., Yao, B., Hu, J., & Fang, X. (2023). Projected increases in emissions of high global warming potential fluorinated gases in China. *Communications Earth & Environment*, *4*(1), 205. https://doi.org/10.1038/s43247-023-00859-6

Harnisch, J. (2000). Atmospheric Perfluorocarbons: Sources and Concentrations. In J. van Ham, A. P. M. Baede, L. A. Meyer, & R. Ybema (Eds.), *Non-CO2 Greenhouse Gases: Scientific Understanding, Control and Implementation: Proceedings of the Second International Symposium,*

Noordwijkerhout, The Netherlands, 8–10 September 1999 (pp. 205–210). Springer Netherlands. https://doi.org/10.1007/978-94-015-9343-4_31

Henne, S., Brunner, D., Groot Zwaaftink, C., & Stohl, A. (2018). *FLEXPART 8-CTM-1.1: Atmospheric Lagrangian Particle Dispersion Model for global tracer transport* (Version 8-CTM-1.1) [Computer software]. Zenodo. https://doi.org/10.5281/zenodo.1249190

Hersbach, H., Bell, B., Berrisford, P., Hirahara, S., Horányi, A., Muñoz-Sabater, J., Nicolas, J., Peubey, C., Radu, R., Schepers, D., Simmons, A., Soci, C., Abdalla, S., Abellan, X., Balsamo, G., Bechtold, P., Biavati, G., Bidlot, J., Bonavita, M., & Thépaut, J.-N. (2020). The ERA5 global reanalysis. *Quarterly Journal of the Royal Meteorological Society*, *146*(730), 1999–2049. https://doi.org/10.1002/qj.3803

Intergovernmental Panel on Climate. (2024). *What is the IPCC?* https://www.ipcc.ch/site/assets/uploads/2024/04/IPCCFactSheet_WhatisIPCC.pdf

Intergovernmental Panel on Climate Change. (2022). *Climate Change 2022: Mitigation of Climate Change. Contribution of Working Group III to the Sixth Assessment Report of the Intergovernmental Panel on Climate Change* (P. R. Shukla, J. Skea, R. Slade, A. A. Khourdajie, R. van Diemen, D. McCollum, M. Pathak, S. Some, P. Vyas, R. Fradera, M. Belkacemi, A. Hasija, G. Lisboa, S. Luz, & J. Malley, Eds.). IPCC. https://www.ipcc.ch/report/ar6/wg3/downloads/report/IPCC_AR6_WGIII_FullReport.pdf

Intergovernmental Panel on Climate Change (IPCC). (1995). *Climate Change 1995: The Science of Climate Change. Contribution of Working Group I to the Second Assessment Report of the IPCC*. Cambridge University Press. https://unfccc.int/process/transparency-and-reporting/greenhouse-gas-data/greenhouse-gas-data-unfccc/global-warming-potentials

International Aluminium Institute. (2020). *2019 Anode Effect Survey Results*. International Aluminium Institute. https://international-aluminium.org/wp-content/uploads/2024/03/2019_anode_effect_survey_result_2020.pdf

International Aluminium Institute. (2024). *Primary Aluminium Production Statistics*. https://archive.international-aluminium.org/statistics/primary-aluminium-production/

International Carbon Action Partnership (ICAP). (2024). *ICAP ETS Map Factsheet*. https://icapcarbonaction.com/system/files/ets_pdfs/icap-etsmap-factsheet-55.pdf

International Institute for Applied System Analysis (IIASA). (2009). *GGI Scenario Database* (Version Ver 2.0) [Dataset]. http://www.iiasa.ac.at/Research/GGI/DB/

International Monetary Fund. (2019). *World Economic Outlook, April 2019: Growth Slowdown, Precarious Recovery*. International Monetary Fund. https://www.imf.org/en/Publications/WEO/Issues/2019/03/28/world-economic-outlook-april-2019

IPCC. (2014). *The Synthesis Report (SYR) of the IPCC Fifth Assessment Report (AR5)* (Assessment Report 5). IPCC. https://www.ipcc.ch/site/assets/uploads/2018/02/SYR_AR5_FINAL_full.pdf

Janssens-Maenhout, G., Crippa, M., Guizzardi, D., Muntean, M., Schaaf, E., Dentener, F., Bergamaschi, P., Pagliari, V., Olivier, J. G. J., Peters, J. A. H. W., van Aardenne, J. A., Monni, S., Doering, U., Petrescu, A. M. R., Solazzo, E., & Oreggioni, G. D. (2019). EDGAR v4.3.2 Global Atlas of the three major greenhouse gas emissions for the period 1970–2012. *Earth System Science Data*, *11*(3), 959–1002. https://doi.org/10.5194/essd-11-959-2019

Jones, A., Thomson, D., Hort, M., & Devenish, B. (2007). The U.K. Met Office's Next-Generation Atmospheric Dispersion Model, NAME III. In C. Borrego & A.-L. Norman (Eds.), *Air Pollution Modeling and Its Application XVII* (pp. 580–589). Springer US.

Jubb, A. M., McGillen, M. R., Portmann, R. W., Daniel, J. S., & Burkholder, J. B. (2015). An atmospheric photochemical source of the persistent greenhouse gas CF_4. *Geophysical Research Letters*, *42*, 9505–9511. https://doi.org/10.1002/2015GL066193

Kim et al., J. (2014). Quantifying aluminum and semiconductor industry perfluorocarbon emissions from atmospheric measurements. *Geophys. Res. Lett.*, *41*, 4787–4794. https://doi.org/doi:10.1002/ 2014GL059783

Kim, J., Thompson, R., Park, H., Bogle, S., Mühle, J., Park, M.-K., & others. (2021). Emissions of tetrafluoromethane (CF_4) and hexafluoroethane (C_2F_6) from East Asia: 2008 to 2019. *Journal of Geophysical Research: Atmospheres*, *126*, e2021JD034888. https://doi.org/10.1029/2021JD034888

Leber, B. P., Tabereaux, A. T., Marks, J., Lamb, B., Howard, T., Kantamaneni, R., Gibbs, M., Bakshi, V., & Dolin, E. J. (2016). Perfluorocarbon (PFC) Generation at Primary Aluminum Smelters. In G. Bearne, M. Dupuis, & G. Tarcy (Eds.), *Essential Readings in Light Metals: Volume 2 Aluminum Reduction Technology* (pp. 1015–1023). Springer International Publishing. https://doi.org/10.1007/978-3-319-48156-2_150

Li, P., & Tanhua, T. (2021). Medusa–Aqua system: Simultaneous measurement and evaluation of novel potential halogenated transient tracers HCFCs, HFCs, and PFCs in the ocean. *Ocean Science*, *17*(2), 509–525. https://doi.org/10.5194/os-17-509-2021

Li, S., & Du, K. (2020). Comparisons of forward-in-time and backward-in-time Lagrangian stochastic dispersion models for micro-scale atmospheric dispersion. *Journal of the Air & Waste Management Association*, *70*(4), 425–435. https://doi.org/10.1080/10962247.2020.1728424

Miller, B. R., Weiss, R. F., Salameh, P. K., Tanhua, T., Greally, B. R., Mühle, J., & Simmonds, P. G. (2008). Medusa: A sample preconcentration and GC/MS detector system for in situ measurements of atmospheric trace halocarbons, hydrocarbons, and sulfur compounds. *Analytical Chemistry*, *80*(5), 1536–1545. https://doi.org/10.1021/ac702084k

Ministry of Environment, Forest and Climate Change (MoEFCC). (2024). *India Fourth Biennial Update Report*. Ministry of Environment, Forest and Climate Change, Government of India. https://unfccc.int/sites/default/files/resource/India%20BUR-4.pdf

Mühle, J., Ganesan, A. L., Miller, B. R., Salameh, P. K., Harth, C. M., Greally, B. R., Rigby, M., Porter, L. W., Steele, L. P., Trudinger, C. M., Krummel, P. B., O'Doherty, S., Fraser, P. J., Simmonds, P. G., Prinn, R. G., & Weiss, R. F. (2010). Perfluorocarbons in the global atmosphere: Tetrafluoromethane, hexafluoroethane, and octafluoropropane. *Atmospheric Chemistry and Physics*, *10*(11), 5145–5164. https://doi.org/10.5194/acp-10-5145-2010

NASA. (2024, October). *First greenhouse gas plumes detected with NASA-designed instrument*. https://phys.org/news/2024-10-greenhouse-gas-plumes-nasa-instrument.html

National Institution for Transforming India (NITI Aayog). (2025). *India Climate and Energy Dashboard*. https://iced.niti.gov.in/energy/end-use/industry/aluminium

Nisbet, E., & Weiss, R. (2010). Top-Down Versus Bottom-Up. *Science*, *328*(5983), 1241–1243. https://doi.org/10.1126/science.1189936

OECD. (2021). *OECD Economic Surveys: Malaysia 2021*. OECD Publishing. https://doi.org/10.1787/cc9499dd-en

Pisso, I., Sollum, E., Grythe, H., Kristiansen, N. I., Cassiani, M., Eckhardt, S., Arnold, D., Morton, D., Thompson, R. L., Groot Zwaaftink, C. D., Evangeliou, N., Sodemann, H., Haimberger, L., Henne, S., Brunner, D., Burkhart, J. F., Fouilloux, A., Brioude, J., Philipp, A., … Stohl, A. (2019). The Lagrangian particle dispersion model FLEXPART version 10.4. *Geoscientific Model Development*, *12*(12), 4955–4997. https://doi.org/10.5194/gmd-12-4955-2019

Prinn, Weiss, R., Arduini, J., Arnold, T., DeWitt, H. L., Fraser, P., Ganesan, A., Gasore, J., Harth, C., Hermansen, O., Kim, J., Krummel, P., Loh, Z., Lunder, C., Maione, M., Manning, A., Miller, B., Mitrevski, B., Mühle, J., … Zhou, L. (2022). *The Advanced Global Atmospheric Gases Experiment (AGAGE) Data*. https://doi.org/10.15485/1841748

Prinn, Weiss, R. F., Fraser, P. J., Simmonds, P. G., Cunnold, D. M., Alyea, F. N., O'Doherty, S., Salameh, P., Miller, B. R., Huang, J., Wang, R. H. J., Hartley, D. E., Harth, C., Steele, L. P., Sturrock, G., Midgley, P. M., & McCulloch, A. (2000). A history of chemically and radiatively important gases in air deduced from ALE/GAGE/AGAGE. *jgr*, *105*(D14), 17,751-17,792. https://doi.org/10.1029/2000JD900141

Püschel, B. E. (2025). *Global Emissions of Hexafluoroethane (C2F6) Determined by Inverse Modelling* [Master's Thesis]. University of Vienna, Institute of Meteorology and Geophysics (IMGW).

Renaud, K. M. (2023). *The Mineral Industry of India, 2017–2018* (Volume III; 2017–2018 Minerals Yearbook,). U.S. Geological Survey. https://pubs.usgs.gov/myb/vol3/2017-18/myb3-2017-18-india.pdf

Say, D., Manning, A. J., Western, L. M., Young, D., Wisher, A., Rigby, M., Reimann, S., Vollmer, M. K., Maione, M., Arduini, J., Krummel, P. B., Mühle, J., Harth, C. M., Evans, B., Weiss, R. F., Prinn, R. G., & O'Doherty, S. (2021). Global trends and European emissions of tetrafluoromethane (CF_4), hexafluoroethane (C_2F_6) and octafluoropropane (C_3F_8). *Atmospheric Chemistry and Physics*, *21*(3), 2149–2164. https://doi.org/10.5194/acp-21-2149-2021

Seibert, P., & Frank, A. (2004). Source-receptor matrix calculation with a Lagrangian particle dispersion model in backward mode. *Atmospheric Chemistry and Physics*, *4*(1), 51–63. https://doi.org/10.5194/acp-4-51-2004

Stohl, A., Cooper, O. R., & James, P. (2004). A Cautionary Note on the Use of Meteorological Analysis Fields for Quantifying Atmospheric Mixing. *Journal of the Atmospheric Sciences*, *61*, 1446–1453.

Tarantola, A. (2005). *Inverse Problem Theory and Methods for Model Parameter Estimation*. Society for Industrial and Applied Mathematics. http://epubs.siam.org/doi/book/10.1137/1.978089871792

Thacker, W. C. (2007). Data assimilation with inequality constraints. *Ocean Modelling*, *16*(3), 264–276. https://doi.org/10.1016/j.ocemod.2006.11.001

Thompson, R. L., & Stohl, A. (2014). FLEXINVERT: an atmospheric Bayesian inversion framework for determining surface fluxes of trace species using an optimized grid. *Geoscientific Model Development*, *7*(5), 2223–2242. https://doi.org/10.5194/gmd-7-2223-2014

Thomson, D. J. (1987). Criteria for the selection of stochastic models of particle trajectories in turbulent flows. *Journal of Fluid Mechanics*, *180*, 529–556. Cambridge Core. https://doi.org/10.1017/S0022112087001940

Trudinger, C. M., Fraser, P. J., Etheridge, D. M., Sturges, W. T., Vollmer, M. K., Rigby, M., Martinerie, P., Mühle, J., Worton, D. R., Krummel, P. B., Steele, L. P., Miller, B. R., Laube, J., Mani, F. S., Rayner, P. J., Harth, C. M., Witrant, E., Blunier, T., Schwander, J., … Battle, M. (2016). Atmospheric abundance and global emissions of perfluorocarbons CF_4, C_2F_6 and C_3F_8 since 1800 inferred from ice core, firn, air archive and in situ measurements. *Atmospheric Chemistry and Physics*, *16*(18), 11733–11754. https://doi.org/10.5194/acp-16-11733-2016

U. S. Environmental Protection Agency (EPA). (1995). *Voluntary Aluminum Industrial Partnership (VAIP)*. https://omb.report/icr/201204-2060-017/doc/31918201.pdf

U. S. Environmental Protection Agency (EPA). (2009). *Mandatory Reporting of Greenhouse Gases Rule*. https://19january2021snapshot.epa.gov/sites/static/files/2014-09/documents/ghg-mrr-final-rule.pdf

United Nations Environment Programme (UNEP). (1987). *1987 Montreal Protocol on Substances that Deplete the Ozone Layer*. https://treaties.un.org/doc/Publication/UNTS/Volume%201522/volume-1522-I-26369-English.pdf

United Nations Environment Programme (UNEP). (2016). *Kigali Amendment to the Montreal Protocol (2016)*. https://ozone.unep.org/treaties/montreal-protocol/amendments/kigali-amendment-2016-amendment-montreal-protocol-agreed

United Nations Framework Convention on Climate. (2015). *Paris Agreement*. https://unfccc.int/sites/default/files/english_paris_agreement.pdf

United Nations Framework Convention on Climate Change. (n.d.). *What is the United Nations Framework Convention on Climate Change?* https://unfccc.int/process-and-meetings/what-is-the-united-nations-framework-convention-on-climate-change

United Nations Framework Convention on Climate Change. (1997, 10.12. , Kyoto). *KYOTO PROTOCOL TO THE UNITED NATIONS FRAMEWORK CONVENTION ON CLIMATE CHANGE*. https://unfccc.int/resource/docs/convkp/kpeng.pdf

United Nations Framework Convention on Climate Change (UNFCCC). (2012). *Doha Amendment to the Kyoto Protocol*. https://unfccc.int/files/kyoto_protocol/application/pdf/kp_doha_amendment_english.pdf

United Nations Framework Convention on Climate Change (UNFCCC). (2024). *National Greenhouse Gas Inventory Data* [Dataset]. https://di.unfccc.int/

United Nations Framework Convention on Climate Change (UNFCCC). (2025). *Guidelines on reporting National Communications*. https://unfccc.int/preparation-of-ncs-and-brs#Guidelines-on-reporting-National-Communications

United States Congress. (1990). *Clean Air Act Amendments of 1990*. https://nepis.epa.gov/Exe/ZyPDF.cgi/900L0400.PDF?Dockey=900L0400.PDF

U.S. Environmental Protection Agency. (1994). Protection of Stratospheric Ozone: Significant New Alternatives Policy (SNAP) Program. *Federal Register*, *59*(53), 13044–13141.

U.S. Environmental Protection Agency. (2018). *Semiconductor Industry Greenhouse Gas Reporting under the GHGRP*.

U.S. Environmental Protection Agency. (2025). *Facility Level Information on Greenhouse Gases Tool (FLIGHT)*. https://ghgdata.epa.gov/ghgp/main.do#/facility/

Verma, P., Verma, A., & Agnihotri, A. (2015). India's initiatives on Improving Energy Efficiency in Aluminium Industries. *Asia Pacific Journal of Energy and Environment*, *2*(2), 63–70.

Vojta, M., Plach, A., Thompson, R. L., & Stohl, A. (2022). A comprehensive evaluation of the use of Lagrangian particle dispersion models for inverse modeling of greenhouse gas emissions. *Geoscientific Model Development*, *15*(22), 8295–8323. https://doi.org/10.5194/gmd-15-8295-2022

Weiss, R., & Prinn, R. (2011). Quantifying greenhouse-gas emissions from atmospheric measurements: A critical reality check for climate legislation. *Philosophical Transactions. Series A, Mathematical, Physical, and Engineering Sciences*, *369*, 1925–1942. https://doi.org/10.1098/rsta.2011.0006

Wong, D. S., Fraser, P., Lavoie, P., & Kim, J. (2015). PFC Emissions from Detected Versus Nondetected Anode Effects in the Aluminum Industry. *JOM*, *67*(2), 342–353. https://doi.org/10.1007/s11837-014-1265-8

World Bank. (2023). *GDP (constant 2015 US$)—United States*. https://data.worldbank.org/indicator/NY.GDP.MKTP.KD?end=2023&locations=OE-US&name_desc=true&start=2023&view=map&year=2015

Yao, B., Vollmer, M. K., Zhou, L. X., Henne, S., Reimann, S., Li, P. C., Wenger, A., & Hill, M. (2012). In-situ measurements of atmospheric hydrofluorocarbons (HFCs) and perfluorocarbons (PFCs) at the Shangdianzi regional background station, China. *Atmospheric Chemistry and Physics*, *12*(21), 10181–10193. https://doi.org/10.5194/acp-12-10181-2012